Study of low-lying proton unbound states in ^{24}Al using the ^{24}Mg(^{3}He, t)^{24}Al reaction.

E. C. Vyfers

A thesis submitted in partial fulfillment of the requirements for the degree of Magister Scientiae.

University of the Western Cape

Faculty of Natural Sciences

Dept. of Physics & Astronomy

2022

To my mother.

Declaration

I, Esmond Craig Vyfers, hereby declare that STUDY OF LOW-LYING PROTON UNBOUND STATES IN ^{24}Al USING THE ^{24}Mg(^{3}He,t)^{24}Al REACTION is my own work, that it has not been submitted for any degree or examination in any other university, and that all the sources I have used or quoted have been indicated and acknowledged by complete references.

Signed:  Date: June 2022

Acknowledgments

As I prepare this thesis for submission, I would like to express my gratitude to my supervisor, Professor Smarajit Triambak, for his guidance and feedback that were crucial to the success of this project. Thank you for being such a great mentor and leaving an indelible impression on me. I sincerely appreciate your time and all the sacrifices you've made towards my academic success.

I thank Vicente Pesudo, who ran the experiment, for fruitful discussions and making himself available to address my questions. I would also like to thank Retief Neveling and Phil Adsley, your help with the sorting code and guidance on the analysis were important to the results obtained in this work. A special thanks goes to Mohamed Kamil for many fruitful discussions on the analysis, over many more drinks. I thank Professor Robbie Lindsay for always going the extra mile to help students overcome obstacles to their academic success, I value your support throughout my studies. I would also like to thank Professor Reggie Madjoe, your determined efforts to extend my funding during this project surely made my final year trouble-free. My sincerest thanks goes to Professor Nico Orce for his continual encouragement and support during my studies.

I thank my office mates for their support during this project. To Bhivek Singh, I appreciate your help with the simulations and the many stimulating discussions on physics. To Jespere Ondze, I'm thankful for your friendship and encouragement. To Bernadette Rebeiro, thank you for setting an excellent example. To Sumeera Gopal, Odwa Tyuka, Lwazikazi Maqungo, and Goitseona Ramonnye, thank you for the positive energy you spread around the office and good luck with your academic endeavors. And to Angela Adams and Sikelela Mqhayi, thank you for going beyond administrative duties to add to an enjoyable M. Sc. experience.

Finally, I am deeply grateful to my mother for all her sacrifices, love and support throughout my life. To my sister, thank you for your support throughout my studies, and being so reliable. To my family, at home and faraway, thank you for all your well wishes during my studies. Last but not least, a very special thanks to my brothers Jermaine Christoffels, Junaid Nolan, Luke Jansen and Brent Cronje for your friendship. I will never forget our adventures, it surely replenished my energies during the challenging times.

Abstract

This MSc project entails a study of astrophysically relevant states in ^{24}Al, that are important for a better understanding of the ^{23}Mg(p,γ)^{24}Al nuclear reaction rate in classical novae. This is a crucial breakout reaction that links the NeNa and MgAl cycles and offers an understanding of the nucleosynthesis of elements between Neon and Aluminium. In this work the $K = 600$ magnetic spectrometer at iThemba LABS was used together with a silicon detector array to measure proton branching ratios for the relevant states in ^{24}Al using the ^{24}Mg(^{3}He,t) charge-exchange reaction. Our experiment yields the first direct measurement of the relative proton branching ratios from these states. We used our measured observables and theoretical estimates of partial gamma widths of unbound states in ^{24}Al, to indirectly determine the total ^{23}Mg(p,γ) reaction rate at nova temperatures.

Contents

1 Introduction **1**

1.1 Stellar evolution . . . 1

1.1.1 Hydrogen & advanced burning cycles . . . 2

1.1.2 Core collapse supernovae . . . 3

1.2 Classical novae . . . 4

1.3 Stellar reaction rates . . . 6

1.3.1 Nonresonant reaction mechanism . . . 6

1.3.2 Resonant reaction mechanism . . . 9

1.3.2.1 Partial widths . . . 12

1.4 Previous work . . . 14

2 Experimental facility **16**

2.1 The QDD spectrometer . . . 17

2.1.1 The drift chambers . . . 18

2.1.2 The scintillator detectors . . . 19

2.2 The silicon detector array . . . 20

3 Data & Analysis **22**

3.1 Targets used . . . 22

3.2 Particle Identification . . . 22

3.3 Energy calibration . . . 26

3.4 Coincidence analysis . . . 30

3.4.1 Energy calibration of CAKE . . . 30

3.4.2 Timing characteristics of CAKE . . . 32

3.4.3 Energies of the proton emitting recoils . . . 34

3.5 Angular distribution of the protons . . . 37

3.5.1 Contamination in the triton spectrum . . . 38

3.5.2 Detection efficiency of CAKE . . . 39

4 Results & Discussion **43**

4.0.1 Level energies of ^{24}Al 43

4.1 Proton branching ratio measurements 44

4.1.1 The ^{23}Mg(p,γ)^{24}Al stellar reaction rate 47

4.2 Conclusions 50

A Focal plane position centroids **51**

B Energy loss of the recoil in the target **54**

List of Figures

1.1 A comparison of luminosities relative to solar, for hydrogen burning stars on the main sequence and their surface temperature. Figure taken from Ref. [2]. 2

1.2 A schematic representation of the reactions of the pp chains where chain 1 is the dominant mode of nuclear processing. The loss percentages shown are due to escaping neutrinos. Figure adapted from Ref. [1]. 3

1.3 A schematic view of an *onion*-like internal structure of a star, with the heaviest elements located at the core. Figure taken from Ref. [2]. 3

1.4 Pictorial representation of a nova outburst produced by a closely orbiting red giant star and a white dwarf [6]. 4

1.5 The CNO cycle shown together with reactions to the NeNa cycle, which opens up the path to the synthesis of heavier elements. Figure taken from Ref. [8]. 5

1.6 The NeNa and MgAl cycles with the crucial $^{23}\mathrm{Mg}(p,\gamma)$ link between the cycles, highlighted by the rectangular box. Figure adapted from Ref. [9]. 5

1.7 The combined potential, for nuclear and Coulomb terms. The effective barrier has height E_c. Picture taken from Ref. [10]. 7

1.8 The Gamow peak for the nuclear reaction rate in a star results from the convolution of the Maxwell-Boltzmann distribution and the tunneling probability through the Coulomb barrier. Figure taken from Ref. [11]. 8

1.9 A schematic representation of a two-step or resonant capture reaction and the subsequent γ-ray emission of the compound nucleus formed by the reaction. Figure taken from Ref. [1]. . 10

2.1 A schematic diagram of the cyclotron facility located at iThemba LABS, South Africa. Figure taken from Ref. [25]. 16

2.2 A schematic diagram of the $K = 600$ QDD magnetic spectrometer at iThemba LABS. Figure reproduced from Ref. [25]. 17

2.3 A cross-sectional top view of a multi-wire drift chamber (MWDC) where the X-wire plane is made up of 198 gold-plated tungsten signal wires interspersed with 199 field-shaping wires of the same material. The U-wire plane, mounted at angle of 50° relative to the scattering plane, is similarly made up of 143 signal wires and 144 guard wires [25]. The Ni-Cr guard wires at the periphery are used to reduce leakage currents by suppressing the spontaneous discharge of electrons. 18
2.4 A scintillator detector coupled to a photomultiplier tube by a light-guide. The PMT converts the energy of incident radiation into a pulse through a series of dynodes that multiply the electrons ejected from the surface of the photocathode. 19
2.5 Position-sensitive drift chambers, with the plastic scintillator paddles at the focal plane of the $K = 600$ spectrometer. Figure taken from Ref. [28]. 20
2.6 *Left*: The geometry of the CAKE array mounted upstream of the target ladder in the scattering chamber with the beam entering from the right. *Right*: The backward facing silicon detector array with a total efficiency ≈ 25 % [26]. 21
2.7 A schematic representation of a DSSSD of the MMM design with 16 ring channels on the junction side and 8 sector channels on the ohmic side. Figure taken from Ref. [26]. 21

3.1 *Left panel*: The particle identification (PID) spectrum for our entire data set, with the thinner MgF_2 target. The triton and deuteron groups are highlighted. *Right panel*: An enhanced view of the PID gate on the triton group, used for the final data analysis. 23
3.2 *Top*: The position spectra for two labeled 1 hour runs without correction. *Bottom*: Aligned position spectra for these runs, because of the offset correction. The inset accentuates the reasonably good alignment that was obtained with this simple correction. 23
3.3 A 2D spectrum of the scattering angle ϑ_{fp}^{scat} versus focal plane position μ, measured by the drift chambers for the entire data set. The narrow vertical loci indicate the improved position resolution obtained through the imposed corrections. The black rectangle selects the astrophysically important state of interest in ^{24}Al at ~ 2345 keV. 24
3.4 Sample triton lineshape fit to a triton peak, accounting for a low-energy tail because of straggling of the tritons. A description of the lineshape function can be found in Ref. [21]. 25
3.5 High-resolution triton spectrum obtained from our experiment. Only peaks below the proton separation energy are labeled here. 25
3.6 A pictorial representation of a binary reaction in the lab and the CM coordinate systems, where a and A represent the ^{3}He projectile and the ^{24}Mg target nucleus, and b and B represent the triton ejectile and ^{24}Al recoil, respectively. 26
3.7 ^{24}Al excitation energies obtained in this work, relative to the values reported in the literature [23, 24, 33, 34]. We use $S_p = 1864$ keV, from measured atomic masses [35]. 29
3.8 α decay chain for the ^{226}Ra source. 30

3.9 *Left panel*: Uncalibrated ring and sector channels of CAKE for the ^{226}Ra source data. *Right panel*: Energy-aligned spectra obtained after the calibrations were performed. 31
3.10 The calibrated spectra for each MMM detector, compared with the gain-matched spectrum of the total CAKE array. 31
3.11 *Left panel*: The TDC channel versus its value for the experimental data with coincidences highlighted by the dashed vertical lines. *Right panel*: The timing distribution with a FWHM $\approx$ 72 channels. 32
3.12 *Left panel*: TDC channels versus the corrected TDC values of the CAKE array. *Right panel*: The corresponding timing distribution that is centered around zero, with a FWHM $\approx$ 43 channels. 33
3.13 The $p-t$ coincidence data, with the proton decay modes of the ^{24}Al nucleus captured by the diagonal bands, where the upper (p_0) and lower (p_1) bands are from transitions to the ground and first excited states in ^{23}Mg, respectively. The ellipse around the p_0 proton group around 2400 keV highlights the lowest ^{23}Mg(p,γ) resonance. 33
3.14 The singles triton energy spectrum of ^{24}Al, overlaid with coincidence data that correspond to the p_0 proton decay mode. We obtain $E_x = 2348(4)$ keV for the first state above $S_p = 1864$ keV. 34
3.15 The angle and energy of ^{24}Al recoils for a range of triton angles in the lab frame. The shaded region indicates these variables at forward angles, up to $\sim 10^\circ$. The inset highlights this region. 35
3.16 A third order polynomial fit to stopping powers versus recoil energies from SRIM, with both nuclear and electronic contributions summed. We used a conservative estimate of 10% relative uncertainty in the stopping powers from SRIM. 36
3.17 A pictorial representation of the in-flight proton decay of the recoil, moving with velocity $\beta' = V_{\rm CM}/c$. 37
3.18 The triton spectra obtained for the MgF_2 and Li_2CO_3 targets. Triton peaks in the former are labeled by A and B. The contamination in the triton spectrum for the MgF_2 target are due to excited states in ^{16}F at 721 and 424 keV labeled by A' and B', with the ground state labeled by C' [43]. 38
3.19 An upstream view of the experimental data for the CAKE array. Note that the CAKE array is not partitioned into the five MMM detectors in this visualization of the data. 40
3.20 A downstream view of the GEANT4 simulated data of the CAKE array with the five MMM detectors partitioned, where the sectors in each MMM detector are clearly visible. The components of CAKE that were not active in the actual experiment were rendered inactive within the simulations. They are shown in this picture with dark boundaries. 40
3.21 Isotropic polar (ϑ) and azimuthal (ϕ) distributions for the registered events, with the five activated detectors of the CAKE array labeled. 41

3.22 The detection efficiency of the rings at backward angles, obtained from a Monte Carlo simulation in GEANT4. Not surprisingly, the innermost ring at $\vartheta \simeq 165^\circ$ has the lowest detection efficiency. 41

4.1 The calibrated spectrum of ^{24}Al up to $E_x \sim 3.5$ MeV. The prominent peaks in ^{24}Al and contamination from the 724 keV state in ^{16}F are labeled. 43

4.2 A Legendre polynomial fit to the angular distribution of the decaying protons that correspond to the first resonance in ^{24}Al. The anisotropy is characterized by the parameters A_2 and A_4. The uncertainties in the coefficients are extracted from the fitting routine, which is based on the Gauss-Jordan elimination technique and also takes into account off-diagonal terms in the covariance matrix. 46

4.3 Legendre polynomial fits to the measured angular distributions of the decaying protons that correspond to the higher-lying resonances in ^{24}Al, labeled by **a**: $E_r = 657(4)$ keV, **b** $E_r = 930(4)$ keV, **c**: $E_r = 1012(4)$ keV and **d**: $E_r = 1117(4)$ keV. 46

4.4 The total ^{23}Mg(p,γ) reaction rate corresponding to four low-lying resonances observed in this work, with the total S-factor for the nonresonant component (DC) adopted from Ref. [20]. . . 49

4.5 The contribution of the direct capture (DC) component and the low-lying resonances to the total ^{23}Mg(p,γ) reaction rate. The uncertainties of the various contributions to the total reaction rate are indicated by the bands. 49

4.6 A comparison of the total ^{23}Mg(p,γ) reaction rate obtained in this work with a previous estimate by Herndl [20], over a range of temperatures from 0.05 GK to 2.5 GK. 50

List of Tables

3.1 Areas obtained from a fit to the α peak around 6000 keV for each MMM detector and its contribution to the gain-matched spectrum of the total CAKE array. 32

4.1 The excitation energies and resonance energies of unbound states in ^{24}Al obtained here, compared with previous work. 45

4.2 The proton branching ratios and resonance strengths obtained in this work, together with shell model calculated values of the partial gamma widths and resonance strengths. 47

A.1 The measured position centroids and areas for the triton events at the focal plane. 53

Chapter 1

Introduction

> We're made of star stuff. We are a way for the Cosmos to know itself.
>
> *Carl Sagan*

The success of the big bang model of the Universe can be attributed to an explanation of the observed helium abundance and the 2.76 K relic radiation from a hot and dense early Universe [1]. It was proposed by Gamow and others that the lighter elements such as ^{2}H, ^{3}He and ^{4}He, were produced during the early expansion of the Universe through the processing of nucleons formed from coalescing quarks at low temperatures [2]. Nucleosynthesis of these light elements drive the early evolution of stars up to the spectacular astrophysical events observed with both terrestrial and space-based telescopes. Some aspects of stellar nucleosynthesis pertinent for this work are discussed below.

1.1 Stellar evolution

When appreciable amounts of hydrogen and helium form a molecular cloud that is stable, star formation is triggered by a compression of this interstellar medium. The gravitational instability of the cloud leads to fragments or protostars in free-fall motion that convert gravitational potential energy into thermal energy. During this early stage of gravitational collapse, a protostar is highly transparent and most of the thermal energy escapes. Nonetheless, the continued collapse of a protostar leads to an increase in its opacity. Eventually, the temperature and density conditions in the core are sufficient to support hydrogen burning. This marks the birth of hydrogen burning stars located on the main sequence of the Hertzsprung-Russell diagram shown in Fig. 1.1. The sequences of nuclear reactions that synthesize helium and produce energy in stars are called proton-proton (pp) chains. The generated energy eventually reaches the surface of a star through radiation, conduction and convection processes [3].

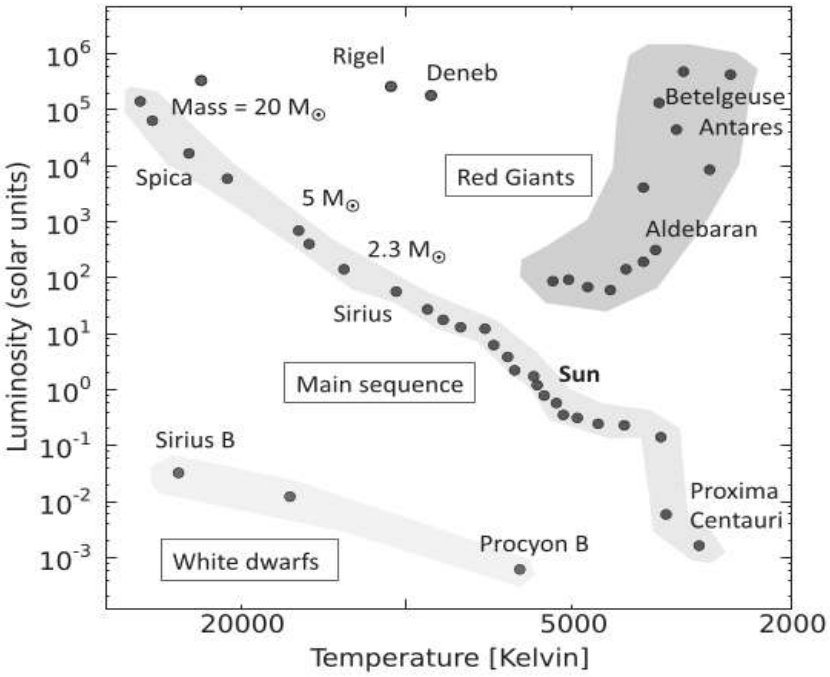

Figure 1.1: A comparison of luminosities relative to solar, for hydrogen burning stars on the main sequence and their surface temperature. Figure taken from Ref. [2].

1.1.1 Hydrogen & advanced burning cycles

Even for stars with appreciable amounts of hydrogen, the probability of four protons simultaneously fusing into a ^{4}He nucleus is extremely small and does not account for the observed luminosities. It was found that sequences of nuclear reactions with two nuclei in the entrance channel are more favorable to effectively fuse hydrogen into helium. The pp chains describing light element creation in the early stage of stellar evolution are illustrated in Fig. 1.2.

During hydrostatic equilibrium, the gravitational collapse of a star is temporarily halted as the gravitational force is counteracted by the gas and radiation pressures due to thermonuclear reactions that occur in the core. This balance is maintained until hydrogen burning can no longer sustain the gravitational weight and a resulting contraction of the core leads to the helium ashes being fused into carbon and oxygen [1]. The interplay between the inward and outward directed forces therefore regulate the contraction of the core and the expansion of the outer regions of the gas throughout the various burning cycles. The heavier elements that are produced settle in the core, with hydrogen and subsequent fuel burning in a spherical shell around it. This layered *onion*-like structure is shown in Fig. 1.3.

[1]The former is through the famous 3α resonance through the Hoyle state in ^{12}C.

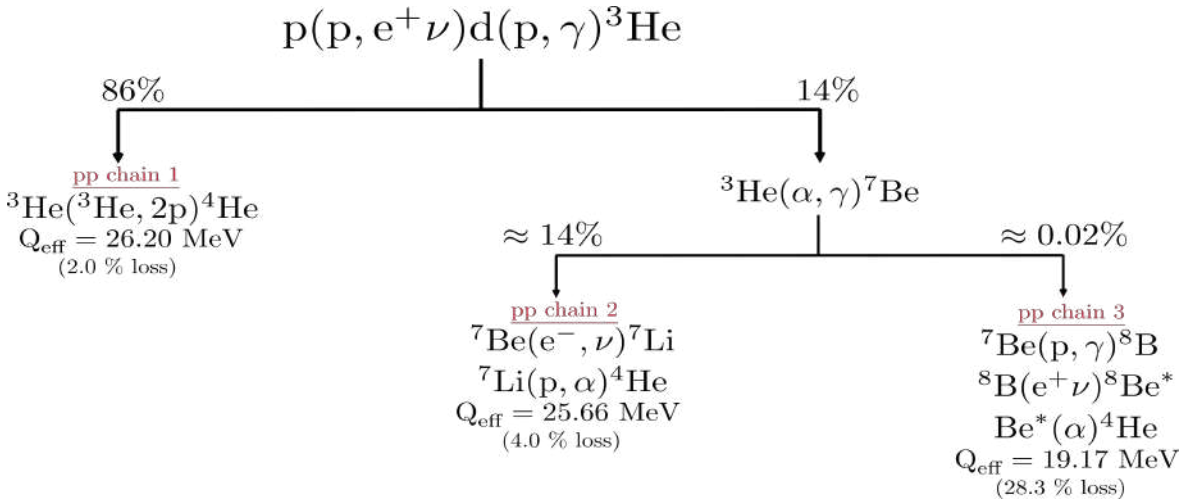

Figure 1.2: A schematic representation of the reactions of the pp chains where chain 1 is the dominant mode of nuclear processing. The loss percentages shown are due to escaping neutrinos. Figure adapted from Ref. [1].

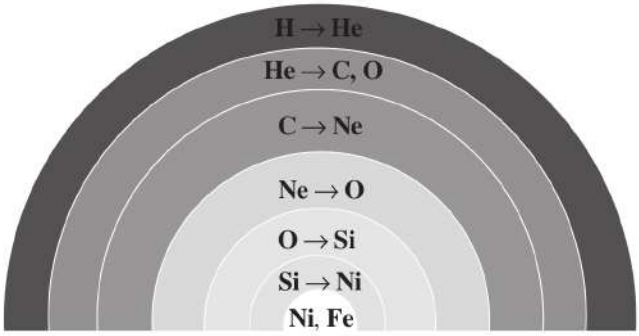

Figure 1.3: A schematic view of an *onion*-like internal structure of a star, with the heaviest elements located at the core. Figure taken from Ref. [2].

1.1.2 Core collapse supernovae

For situations where the mass of the protostar exceeds the Chandrasekhar limit (around 1.4 $M_\odot$), the star becomes unstable against core collapse [4]. At later stages of stellar evolution, the immense gravitational force overcomes the radiative and electron degeneracy pressure within the star. This triggers gravitational collapse, which drives the temperature and density of the iron core up to nuclear densities $\sim 2 \times 10^{14}$ g cm^{-3} [5]. At these extreme densities, the strong repulsive nuclear force dramatically stiffens the equation-of-state (EOS) of the iron core and generates a shock wave that propagates outward. The shock wave prompts a photo-dissociation of iron-peak nuclei. Further electron capture decays lead to a reduction in the electron degeneracy pressure and a removal of energy via neutrino emission. This energy loss leads to a collapse of the iron core that leads to an enormous explosion of the outer envelope of the star. The elements in the regions that envelop the core collide with the shock wave and are violently ejected into the interstellar medium in

this supernova event (SNII). Alternatively, for medium-mass stars with masses < 1.4 $M_{\odot}$, the gravitational weight of the star is supported by the electron degeneracy pressure. The endpoint of stellar evolution in such a scenario is characterized by a degenerate white dwarf. We will now be concerned with the gravitational interaction of such compact objects with hydrogen-rich, main-sequence stars, to form binary systems.

1.2 Classical novae

The co-evolution of binary members are determined by transfer of mass from the hydrogen-rich companion via Roche lobe overflow as it expands into a red giant. The matter from the red giant flows into an accretion disk, spiraling onto the surface of the white dwarf. The high density of the compact star causes an accretion of material at very high velocities, which leads to a rapid thermonuclear runaway. This is characterized by a violent release of energy that ejects synthesized material into interstellar space. Such nova outbursts on the surface of white dwarfs are observationally characterized by a rapid increase in the luminosity of a star, shown pictorially in Fig. 1.4.

Figure 1.4: Pictorial representation of a nova outburst produced by a closely orbiting red giant star and a white dwarf [6].

An important class of classical nova explosions are oxygen-neon (ONe) novae, classified by the oxygen-neon composition of the white dwarf core. In nova explosions, hydrogen burning occurs via the hot CNO cycle which is dominated by (p, γ) type reactions. This is an important mode of nucleosynthesis reaching peak temperatures around $0.3 - 0.4$ GK, with the heavier nuclei participating as catalysts for further nucleosynthetic reactions [7]. The complexity of the CNO cycle is captured in Fig. 1.5.

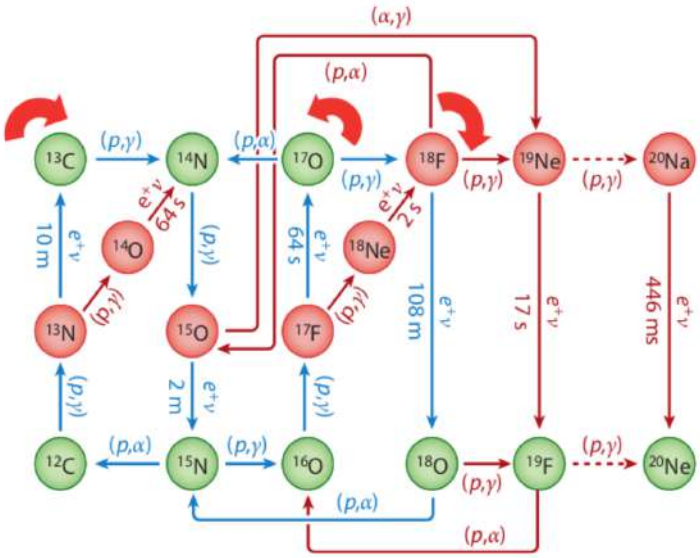

Figure 1.5: The CNO cycle shown together with reactions to the NeNa cycle, which opens up the path to the synthesis of heavier elements. Figure taken from Ref. [8].

As shown above, catalytic material can leak from the hot CNO cycle to produce ^{20}Ne, which forms the basis of the NeNa cycle. The reaction flow through the NeNa cycle can then be altered to the MgAl cycles, through the ^{23}Mg(p,γ) breakout reaction. This is a critical reaction that links the NeNa and MgAl cycles, shown in Fig. 1.6.

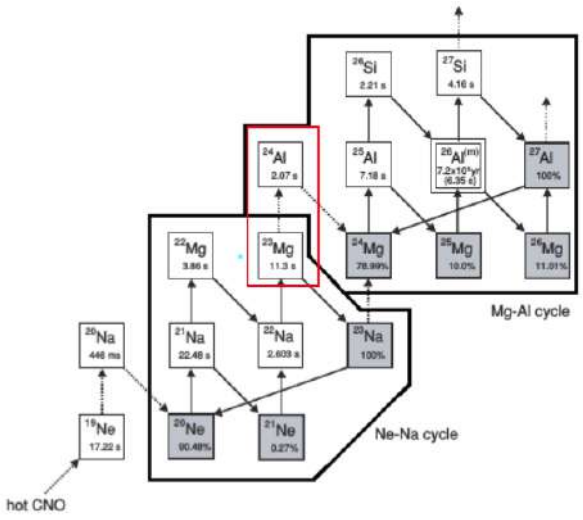

Figure 1.6: The NeNa and MgAl cycles with the crucial ^{23}Mg(p,γ) link between the cycles, highlighted by the rectangular box. Figure adapted from Ref. [9].

Although the sequences of reactions in these cycles are relatively unimportant as a source of energy production in stars (due to the high Coulomb barriers involved), these cycles are important for the nucleosynthesis of elements between ^{20}Ne and ^{27}Al [1]. In this context, an improved understanding of the observed elemental abundances requires an accurate measurement of the ^{23}Mg(p,γ) reaction rate, which remains a critical input in ONe nova models. The reaction rate is dominated by both non-resonant and resonant components, which I describe below.

1.3 Stellar reaction rates

The relative velocity v of the pairs of interacting nuclei N_a and N_b in degenerate stellar matter is described by the Maxwell-Boltzmann distribution

$$\phi(v) = 4\pi v^2 \left(\frac{\mu}{2\pi kT}\right)^{3/2} \exp\left(-\frac{\mu v^2}{2kT}\right), \tag{1.1}$$

where T is temperature of the gas, k is the Boltzmann constant and $\mu = m_1 m_2/(m_1 + m_2)$ is the reduced mass of the interacting nuclei [1]. This expression must be folded with the cross section for a nuclear reaction to arrive at the reaction rate per particle pair

$$\langle \sigma v \rangle = \int_0^\infty \phi(v) v \sigma(v) dv, \tag{1.2}$$

averaged over the velocity distribution.

1.3.1 Nonresonant reaction mechanism

The interaction of nuclei with positive charges Z_1 and Z_2, separated by a distance r is described by the Coulomb potential

$$V_C = \frac{Z_1 Z_2 e^2}{r}. \tag{1.3}$$

This Coulomb barrier significantly inhibits nuclear reactions at low energies $E \ll E_C$, where E_C is the effective height of the combined nuclear and Coulomb potential, shown in Fig. 1.7. The probability of tunneling through the barrier is small, given by the ratio of $|\psi(R_n)|^2/|\psi(R_C)|^2$, where R_n is the sum of the radii for projectile and target nuclei and R_C is the classical turning point. At low energies $E \ll E_C$, this penetrability is given by

$$P = \exp(-2\pi\eta), \tag{1.4}$$

where the Sommerfeld parameter is $\eta = \frac{Z_1 Z_2 e^2}{\hbar v}$.

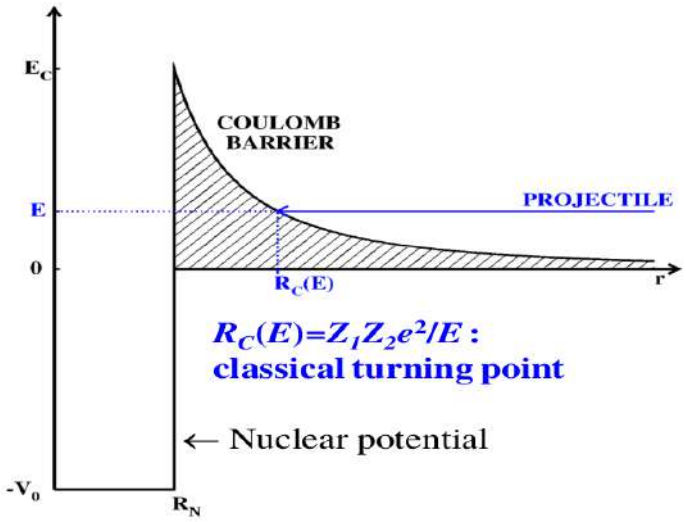

Figure 1.7: The combined potential, for nuclear and Coulomb terms. The effective barrier has height E_c. Picture taken from Ref. [10].

The energy dependent cross section $\sigma(E) \propto \pi\lambda\!\!\!^{-2} \propto 1/E$, where $\lambda\!\!\!^{-}$ is the reduced de Broglie wavelength, and $\sigma(E) \propto \exp(-2\pi\eta)$. One can then define [1]

$$\sigma(E) = \frac{1}{E}\exp(-2\pi\eta)S(E), \tag{1.5}$$

where $S(E)$ is the astrophysical S-factor that contains all the nuclear physics related information for the reaction [1]. Using the non-relativistic relation $p = (2m_pE_p)^{1/2}$ and $p = \hbar k$ where k is the wave number, we obtain the reduced de Broglie wavelength as

$$\lambda\!\!\!^{-} = \frac{\hbar}{\sqrt{2m_pE_p}}, \tag{1.6}$$

where m_p and E_p are the mass and the kinetic energy of the projectile, respectively.

Using Eq. (1.2) and writing out separately the Maxwellian velocity distributions of the two interacting nuclei in terms of the center-of-mass velocity V and the relative velocity v, the reaction rate per particle pair simplifies to

$$\langle\sigma v\rangle = \int_0^\infty \int_0^\infty \phi(V)\phi(v)\sigma(v)v dV dv. \tag{1.7}$$

One can further integrate this expression over V to obtain

$$\langle\sigma v\rangle = 4\pi\left(\frac{\mu}{2\pi kT}\right)^{3/2}\int_0^\infty v^3\sigma(v)\exp\left(-\frac{\mu v^2}{2kT}\right)dv, \tag{1.8}$$

which together with the relation $E = \frac{1}{2}\mu v^2$ such that, $v^3dv = \left(\frac{2E}{\mu^2}\right)dE$ gives

$$\langle \sigma v \rangle = \left(\frac{8}{\pi\mu}\right)^{1/2} \frac{1}{(kT)^{3/2}} \int_0^\infty \sigma(E) E \exp\left(-\frac{E}{kT}\right) dE. \tag{1.9}$$

This, together with Eq. (1.5) and assuming that the S-factor is a slowly varying function (for non-resonant reactions) around the effective burning energy E_0 leads to

$$\langle \sigma v \rangle = \left(\frac{8}{\pi\mu}\right)^{1/2} \frac{1}{(kT)^{3/2}} S(E_0) \int_0^\infty \exp\left(-\frac{E}{kT} - 2\pi\eta\right) dE. \tag{1.10}$$

The penetrability through the Coulomb barrier can be described in terms of a term $b = (2\mu)^{1/2} \pi e^2 Z_1 Z_2/\hbar$ [1], such that

$$2\pi\eta = \frac{b}{\sqrt{E}}. \tag{1.11}$$

This leads to [1]

$$\langle \sigma v \rangle = \left(\frac{8}{\pi\mu}\right)^{1/2} \frac{1}{(kT)^{3/2}} S(E_0) \int_0^\infty \exp\left[-\frac{E}{kT} - \frac{b}{\sqrt{E}}\right] dE. \tag{1.12}$$

The convolution of the dominant energy-dependent functions in Eq. (1.12) give rise to the Gamow peak, with a sufficiently high probability for the reaction to occur near E_0, as shown in Fig. 1.8.

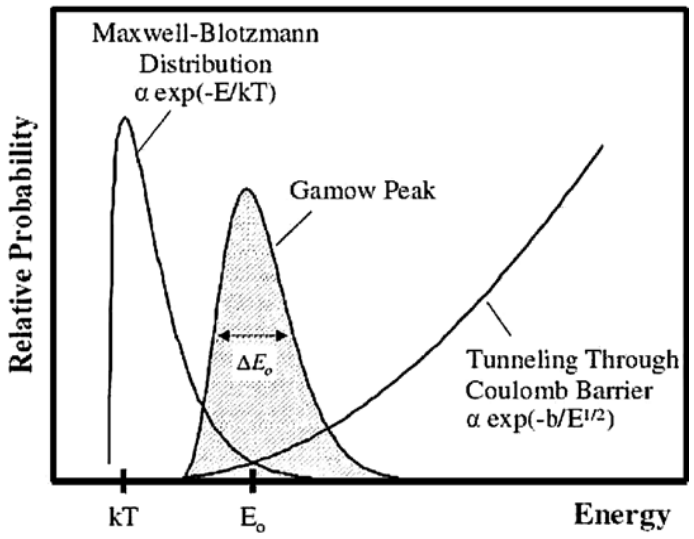

Figure 1.8: The Gamow peak for the nuclear reaction rate in a star results from the convolution of the Maxwell-Boltzmann distribution and the tunneling probability through the Coulomb barrier. Figure taken from Ref. [11].

Therefore, at a given temperature T, nuclear reactions occur in a narrow energy window around the effective burning energy E_0, where the integrand in Eq. (1.12) has a maximum value. One obtains E_0 to be

$$E_0 = \left(\frac{bkT}{2}\right)^{2/3}. \tag{1.13}$$

By substituting Eq. (1.13) into Eq. (1.12) and evaluating the integral, we obtain for the maximum value for the integrand

$$\begin{aligned} I_{max} &= \exp\left(-\frac{E_0}{kT} - \frac{b}{\sqrt{E_0}}\right) \\ &= \exp\left(-\frac{3E_0}{kT}\right). \end{aligned} \tag{1.14}$$

The effective width of the Gamow peak can be determined by approximating the exponential term in Eq. (1.12) with a Gaussian function [1, 4]

$$\exp\left(-\frac{E}{kT} - \frac{b}{\sqrt{E}}\right) = I_{max} \exp\left[-\left(\frac{E - E_0}{\Delta/2}\right)^2\right], \tag{1.15}$$

where

$$\Delta = \frac{4}{3^{1/2}} \left(E_0 kT\right)^{1/2}. \tag{1.16}$$

This approximation results in the final form of the nuclear reaction rate per particle pair for non-resonant reactions

$$\langle \sigma v \rangle = \left(\frac{2}{\mu}\right)^{1/2} \frac{\Delta}{(kT)^{3/2}} S(E_0) \exp\left(-\frac{3E_0}{kT}\right). \tag{1.17}$$

1.3.2 Resonant reaction mechanism

Compared to non-resonant reactions that show a smoothly varying cross section as a function of energy, resonant reactions are characterized by a significant increase in the cross section at resonant energies. This occurs when the energy in the incoming channel $Q + E_p^{\mathrm{CM}}$ (with E_p^{CM} being the energy of the projectile in the center of mass) matches the excitation energy of a state in the compound nucleus that is formed by the reaction. Such a resonant reaction is shown pictorially in Fig. 1.9.

Cross sections for resonant nuclear reactions can be determined by assuming

$$\sigma(E) \propto \frac{\Gamma_a \Gamma_b}{(E - E_r)^2 + \Gamma^2/4}, \tag{1.18}$$

where Γ_a and Γ_b are the partial widths of the resonant level, and characterize the probability of forming an excited state and its subsequent decays. The total width of the resonance is $\Gamma = \Gamma_a + \Gamma_b$, which is related to the lifetime of the state through $\Gamma\tau = \hbar$. The above relations are better understood using the following arguments. Any excited level has to exponentially decay, following the radioactive decay law

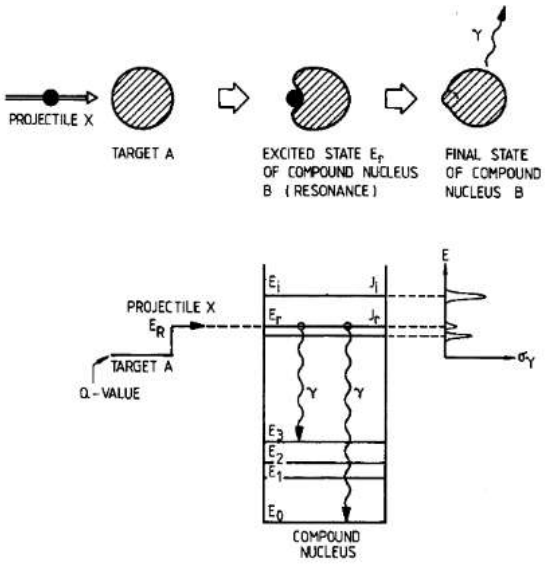

Figure 1.9: A schematic representation of a two-step or resonant capture reaction and the subsequent γ-ray emission of the compound nucleus formed by the reaction. Figure taken from Ref. [1].

$$N(t) = N_0 e^{-\lambda t}. \tag{1.19}$$

Such exponential decay is only possible if the time dependent wave function describing the state is described as

$$\psi(t) = \psi(0) \exp\left(-\frac{i(E_r - \frac{1}{2}i\Gamma)t}{\hbar}\right), \tag{1.20}$$

where E_r is the energy level of interest. The complex energy $E_r - \frac{1}{2}i\Gamma$ is a damping factor added to the stationary state solutions that results in exponential decays. This yields a time evolution

$$|\psi(t)|^2 = |\psi(0)|^2 \exp\left(-\frac{\Gamma t}{\hbar}\right). \tag{1.21}$$

Comparing Eqs. (1.19) and (1.21), it is easy to see that if $\frac{1}{\tau} = \lambda$, where τ is the lifetime of the state, then $\Gamma\tau = \hbar$. This relation clearly shows that states that decay need a finite width in energy. One can apply a Fourier transform to $\psi(t)$ to take it to the energy domain, so that

$$\psi(\omega) = (2\pi)^{-1/2} \int_{-\infty}^{+\infty} \psi(t) \exp(+i\omega t) dt. \tag{1.22}$$

Substitution of $\psi(t)$ into Eq. (1.22), results in the following expressions

$$\begin{aligned}\psi(\omega) &= \frac{\psi(0)}{\sqrt{2\pi}} \int_0^{+\infty} \exp\left(-\frac{iE_r t}{\hbar}\right) \exp\left(\frac{-\Gamma t}{2\hbar}\right) \exp(i\omega t) dt \\ &= \int_0^{+\infty} \exp\left[\frac{i}{\hbar}\left(\hbar\omega - E_r + \frac{i\Gamma}{2}\right) t\right] dt.\end{aligned} \tag{1.23}$$

Since the probability of the particle having energy E is $\propto |\psi(\omega)|^2$, the above expression shows that the energy distribution of an excited nuclear level is

$$P(E) \propto \frac{\Gamma}{(E - E_r)^2 + \Gamma^2/4}, \tag{1.24}$$

where Γ is its Lorentzian or Breit-Wigner width. As shown in Fig. 1.9, a resonant nuclear reaction involves the population of an excited state in the compound nucleus through a two-step process that involves the formation of the state and its decay. It is therefore understandable that the cross section for γ-ray emission (Fig. 1.9) is

$$\sigma_\gamma \propto \Gamma_a \Gamma_b, \tag{1.25}$$

where Γ_a and Γ_b are the partial widths of the compound nuclear (resonant) state. This (together with Eq. (1.24)) justifies Eq. (1.18). For particles with spin, one requires an additional statistical factor ω,

$$\omega = \frac{2J + 1}{(2J_a + 1)(2J_b + 1)}, \tag{1.26}$$

where j_a, j_b and J are the spins of the projectile, the target and the resonance, respectively. For narrow resonances with $\Gamma \ll E_r$, the above formalism leads to

$$\langle \sigma v \rangle = \left(\frac{8}{\pi\mu}\right)^{1/2} \frac{1}{(kT)^{3/2}} E_r \exp\left(-\frac{E_r}{kT}\right) \omega \Gamma_a \Gamma_b \int_0^\infty \frac{\pi \lambda\!\!\!^{-2}}{(E - E_r)^2 + \Gamma^2/4} dE. \tag{1.27}$$

This expression further simplifies to

$$\langle \sigma v \rangle = \left(\frac{8}{\pi\mu}\right)^{1/2} \frac{1}{(kT)^{3/2}} E_r \exp\left(-\frac{E_r}{kT}\right) \omega \Gamma_a \Gamma_b \frac{\hbar^2}{2\mu E_r} \int_0^\infty \frac{1}{(E - E_r)^2 + \Gamma^2/4} dE. \tag{1.28}$$

The value of the integral above is equal to $2\pi/\Gamma$ [1, 12]. Substituting this value and defining the resonance strength $(\omega\gamma)_r$ as the product of the statistical factor ω and the width ratio $\gamma = \Gamma_a \Gamma_b / \Gamma$, one obtains the total resonant rate per particle pair

$$\langle \sigma v \rangle = \left(\frac{2\pi}{\mu kT}\right)^{3/2} \hbar^2 \sum_r (\omega\gamma)_r \, e^{-E_r/kT}, \tag{1.29}$$

where the summation is over all isolated and narrow resonances r. The nuclear physics input that enter into the calculation of a resonant reaction rate are the location of the resonance E_r and the resonance strength $\omega\gamma$. For the rate of the ^{23}Mg$(p,\gamma)^{24}$Al resonance reaction of interest, we have $\Gamma_a = \Gamma_p$ and $\Gamma_b = \Gamma_\gamma$ that determine the resonance strength for each resonance. Below is a brief discussion on such partial proton and gamma widths.

1.3.2.1 Partial widths

The observed resonances of nuclear states are solutions to the Schrödinger equation where the total nuclear wave function is characterized by a rapid variation with energy in the vicinity of a resonance. Such resonance phenomena occur when the interior and the exterior wave functions χ_{in} and χ_{out} match at the nuclear surface of the compound nucleus [4]. This continuity condition is expressed by the logarithmic derivative f, which has the same value for the radial wave functions and their derivatives at the surface and is defined by [4]

$$f = R\left(\frac{1}{\chi(r)}\frac{d\chi(r)}{dr}\right)_{r=\text{R}}. \tag{1.30}$$

An equivalent expression for f in the terms of quantities of the nuclear exterior, the shift factor S and the penetration factor P, is given by [4]

$$f \equiv S + iP. \tag{1.31}$$

To estimate the proton partial width, we consider one open nucleon channel and assume the existence of a well-defined spherical surface at R, and that the projectile and target nuclei have no interaction outside of this radius. The proton partial width Γ_p can then be determined from the proton decay probability of the compound state λ_p through

$$\Gamma_p = \lambda_p \hbar, \tag{1.32}$$

where λ_p is given by the product of the probability of the protons at the nuclear surface and their flux. This product is characterized by the current density given by [4, 13]

$$j = \frac{\hbar}{2\mu i}\left[\chi(r)^*\frac{d\chi(r)}{dr} - \frac{d\chi(r)^*}{dr}\chi(r)\right], \tag{1.33}$$

that can be integrated through a sphere of radius $r \to \infty$ over the full solid angle $d\Omega$ to obtain λ_p. Using $\chi(r) = Y(\theta,\phi)\frac{\chi_c}{r}$ where $Y(\theta,\phi)$ is the spherical harmonic that contains the angular part of the wave function and χ_c is the radial wave function of the compound state, we obtain

$$\begin{aligned}
\lambda_p &= \int_{d\Omega} R^2 j\, d\Omega \\
&= \frac{\hbar}{2\mu i}\int_{d\Omega} R^2\left[\chi(r)^*\frac{d\chi(r)}{dr} - \frac{d\chi(r)^*}{dr}\chi(r)\right]_{r=\text{R}} d\Omega \\
&= \frac{\hbar}{2\mu i}\left(\chi_c^*\frac{d\chi_c}{dr} - \frac{d\chi_c^*}{dr}\chi_c\right),
\end{aligned} \tag{1.34}$$

since $\int_{d\Omega}|Y(\theta,\phi)|^2 d\Omega = 1$. In the compound nucleus description, the observed resonances can be described as a linear combination of the single-particle states p of the interacting nucleons that form the compound state [4].

This is given by

$$\chi_c = \sum_p A_{sp}\chi_{sp}, \tag{1.35}$$

where χ_{sp} is the wave function of a nucleon in the single-particle potential. At a resonance r, the compound state is then described as

$$\chi_c \approx A_{sp}\chi_{sp}, \tag{1.36}$$

since A_{sp} mainly contributes to the wave function of the compound state. Rearranging Eq. (1.30) so that

$$\left(\frac{d\chi(r)}{dr}\right)_{r=\mathrm{R}} = \frac{\chi f}{R}, \tag{1.37}$$

and using Eq. (1.36), the decay probability becomes (see Eq. (1.34))

$$\begin{aligned} \lambda_p &= \frac{\hbar}{2\mu i R}\left(\chi_c^*\chi_c f - f^*\chi_c^*\chi_c\right) \\ &= \frac{\hbar|\chi_{sp}|^2}{2\mu i R}A_{sp}^2\left(f - f^*\right). \end{aligned} \tag{1.38}$$

Together with Eq. (1.32) and Eq. (1.31), this results in an expression for the proton width

$$\begin{aligned} \Gamma_p &= \frac{\hbar^2|\chi_{sp}|^2}{2\mu i R}A_{sp}^2\left[(S+iP) - (S-iP)\right] \\ &= \frac{\hbar^2}{\mu R}A_{sp}^2|\chi_{sp}|^2 P. \end{aligned} \tag{1.39}$$

By introducing the single-particle partial width given by [4]

$$\Gamma_{sp} = \frac{2\hbar^2}{\mu R^2}P\theta_p^2, \tag{1.40}$$

where $\theta_p^2 = \frac{R}{2}|\chi_{sp}|^2$ is a dimensionless single-particle reduced width and making the substitution $C^2S = A_{sp}^2$ for the spectroscopic factor (that characterizes the probability of the nucleons arranging themselves into a particular configuration), the proton partial width can be defined as

$$\Gamma_p = (C^2S)\Gamma_{sp}, \tag{1.41}$$

where C is a Clebsch-Gordan coefficient. For the situation where the compound nucleus can decay by emitting a γ-ray with energy E_γ, the additional decay channel characterized by a width Γ_γ must be considered. The energy-dependence of this width is given by

$$\Gamma_\gamma = \alpha_L E_\gamma^{2L+1}, \tag{1.42}$$

where α_L is a constant and L refers to the multipolarity of the emitted radiation [1].

An estimate of the energy-dependent proton width described above can be obtained from a nuclear shell model calculation by assuming that the proton capture proceeds directly to a single-particle orbit, characterized by the quantum numbers $\{n, l_i, l_f\}$. Here n is the principal quantum number of the single-particle orbit with orbital angular momentum l_f, and l_i is the orbital angular momentum of the scattering wave function [14]. The measured and calculated direct capture cross sections are related through

$$\sigma_{\mathrm{DC}}^{\mathrm{exp}} = C^2 S \sum_{l_i} \sigma_{\mathrm{DC}}^{\mathrm{calc}}(n, l_i, l_f). \tag{1.43}$$

The bound state wave function can be generated using a potential that includes a Coulomb term and a Woods-Saxon term with depth V_0, which reproduce the binding energies of the final state. The scattering wave function can be generated using a suitable scattering potential. In some cases, the same potential model is used to generate both wave functions. As mentioned previously, the spectroscopic factor allows an estimate of the proton width by evaluating the single-particle width (see Eq. (1.40)) using the relevant potential parameters. One can also obtain an estimate of γ-ray partial widths using similar arguments and therefore obtain an estimate of the resonance strength $(\omega\gamma)_r$.

This concludes our discussion of the nuclear physics input for the astrophysically relevant $^{23}\mathrm{Mg}(p,\gamma)^{24}\mathrm{Al}$ reaction. In the absence of direct measurements, accurate determinations of partial widths and lifetimes for the resonant levels play an important role towards a better understanding of astrophysically relevant reaction rates. For the $^{23}\mathrm{Mg}(p,\gamma)^{24}\mathrm{Al}$ reaction, the lowest-lying resonance in $^{24}\mathrm{Al}$ has stimulated several experimental efforts to measure its energy and strength, as this resonance dominates the total reaction rate at nova temperatures. In the following section I provide the current status of the reaction rate by surveying previous work done in this context.

1.4 Previous work

A direct measurement of the lowest-lying $^{23}\mathrm{Mg}(p,\gamma)$ resonance presents an experimental challenge due to the extremely small reaction cross section at astrophysical energies. The earliest work by Wallace *et al.* [15] considers a single resonance at $E_r = 510$ keV, with $E_x = 2380$ keV obtained from tabulated nuclear data [16]. Due to a lack of spectroscopic information regarding this state, the resonance strength was estimated by assuming $C^2S = 0.1$, to obtain $\Gamma_p = 230$ eV and further assuming $\Gamma_\gamma = 0.01$ eV from a systematic study of neighboring nuclei in the mass region. These estimates yielded a resonance strength of ≈ 10 meV. However, in order to obtain a more reliable determination of the reaction rate, more than one resonance must be considered in addition to the direct capture cross section that is significant at lower temperatures ($T < 2$ GK). Such an analysis was performed by Wiescher *et al.* [17]. Later on, Greenfield *et al.* [18] used the $^{24}\mathrm{Mg}(^3\mathrm{He}, t)^{24}\mathrm{Al}$ reaction to obtain $E_x = 2369(4)$ keV for the lowest resonance.

However, this work could not unambiguously determine the spin of this state, which led to a large uncertainty in the extracted reaction rate. Furthermore, an independent measurement using the same reaction [19] obtained a much lower value of $E_x = 2328(10)$ keV, that corresponds to a resonance energy of 458(10) keV. Its spin-parity value was determined to be $J^\pi = 3^+$ from the angular distributions of the tritons. Herndl. *et al.* [20] attempted to resolve the discrepant level energies above by using all available experimental information for ^{24}Al together with the isobaric multiplet mass equation (IMME) [21, 22]. They assumed $J^\pi = 3^+$ for the resonance and extracted a lower precision value for the excitation energy $E_x = 2349(20)$ keV, which agreed with both Refs. [18, 19]. Consequently, the determined resonance energy had a large uncertainty, with $E_r = 478(20)$ keV, which can be explained by the *inconsistent* measured values for the excitation energies [23]. Furthermore, Ref. [20] obtained the partial widths of the unbound states from shell model calculations, with $\Gamma_p = 0.185$ eV and $\Gamma_\gamma = 0.033$ eV. This results in a calculated resonance strength $\omega\gamma = 25$ meV.

More recently, a ^{24}Mg(^{3}He, t)^{24}Al study by Visser *et al.* [23] obtained $E_x = 2346(6)$ keV, which agreed with the value quoted by Ref. [20]. This leads to a more precise value for the resonance energy, $E_r = 474(6)$ keV, which reduced the uncertainty in the reaction rate by about a factor of 3 [23]. An independent study by Lotay *et al.* [24], using γ-ray spectroscopy now yields the most precisely determined value for the 3^+ state at $E_x = 2345.1(14)$ keV, in agreement with the values obtained by Refs. [20, 23].

The only direct measurement of the resonance strength was performed at TRIUMF [9], with a radioactive ^{23}Mg beam incident on a gas target. The recoils from the reaction were focused on the focal plane of the DRAGON spectrometer and used to directly determine the reaction rate [9]. However, this experiment was plagued by beam contamination and other experimental challenges associated with the use of gas targets. Hence, the resonance strength could only be determined with a large uncertainty, with $\omega\gamma = 37.8^{+20.5}_{-15.4}$ meV.

It is clear from the above that more work needs to be done to better constrain the ^{23}Mg(p, γ)^{24}Al reaction rate. The work in this thesis is mainly aimed at obtaining a precise measurement of the proton branch of the lowest-lying unbound state in ^{24}Al. In the next chapter I describe the equipment used for the measurement, using the ^{24}Mg(^{3}He, t)^{24}Al charge-exchange reaction.

Chapter 2

Experimental facility

The ^{24}Mg(^{3}He, t)^{24}Al experiment was performed at the iThemba LABS accelerator facility, shown in Fig. 2.1.

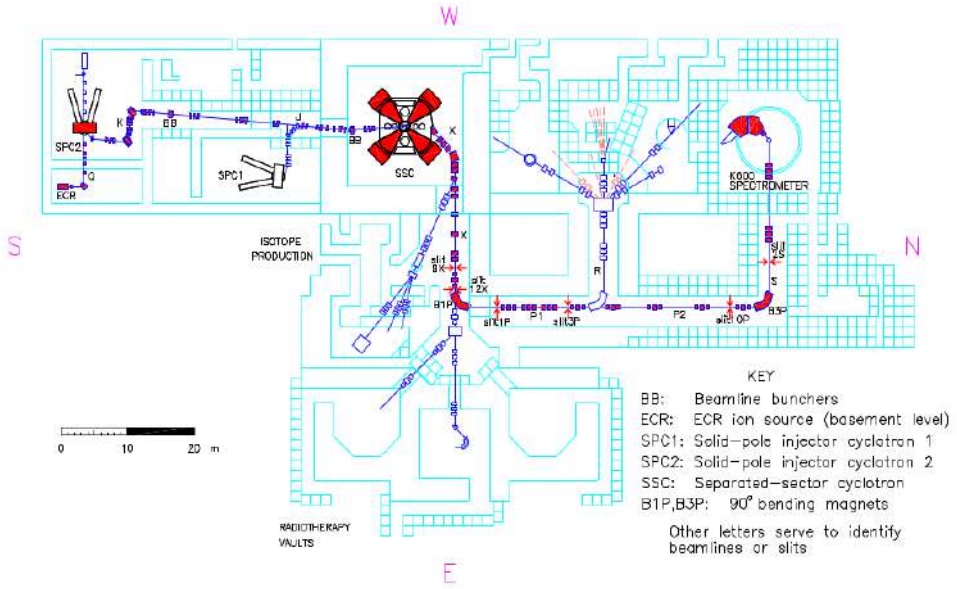

Figure 2.1: A schematic diagram of the cyclotron facility located at iThemba LABS, South Africa. Figure taken from Ref. [25].

We produced excited states in ^{24}Al by bombarding a $\sim$ 200 μg/cm^2 thick MgF_2 target with a 50 MeV ^{3}He^{2+} beam provided by the Separated Sector Cyclotron (SSC) after pre-accelerating the positive ions produced at an Electron Cyclotron Resonance (ECR) ion source. An oscillatory field was provided by a RF power supply, so that the ions traversed the cyclotron with a revolution frequency [1]

$$f = \frac{qB}{2\pi m}, \tag{2.1}$$

where q is the charge state of the ion with mass m, in a magnetic field B [1].

For an ion bunch traversing the acceleration gap N-times, the extracted ions had beam energy $E = NqV$, where V is the potential difference between the dee electrodes of the SSC accelerating structure. The emerging ions were then directed onto the target placed in the scattering chamber, where the reaction products were momentum analyzed with the $K = 600$ magnetic spectrometer [25], shown in Fig. 2.2.

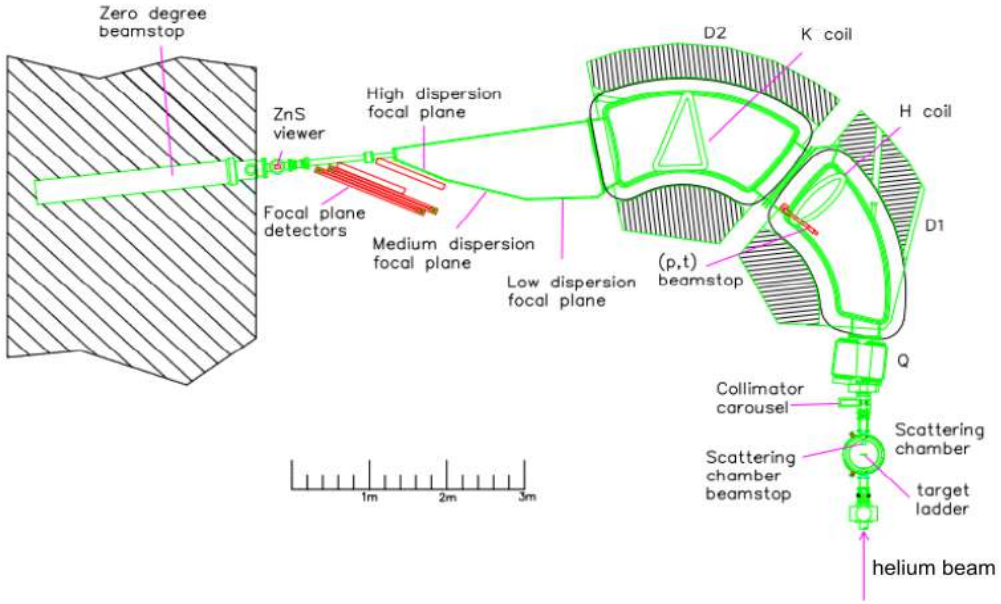

Figure 2.2: A schematic diagram of the $K = 600$ QDD magnetic spectrometer at iThemba LABS. Figure reproduced from Ref. [25].

In the following sections I briefly describe the active elements of the magnetic spectrometer, its focal plane detectors and a silicon detector array, placed upstream of the target to perform coincidence spectroscopy of the unbound protons from ^{24}Al.

2.1 The QDD spectrometer

The scattering chamber at the turning axis of the spectrometer hosts a ladder with six target positions and an array of Double Sided Silicon Strip Detectors (DSSSD) mounted upstream of the target, in a 'lampshade' configuration. Following a nuclear reaction in the scattering chamber, the ejectiles were momentum analyzed and detected through coincidences between the drift chambers and plastic scintillator detectors at the focal plane. The quadrupole magnet at the entrance of the spectrometer focused these ejectiles, with their dispersion in momentum ($\Delta p/p$) set adjusted by the fields of the dipole magnets D1 and D2. Further focusing is aided by trim coils located inside these dipole magnets.

The experiment was performed with the spectrometer operating in zero-degree mode [25, 26], with the spectrometer acceptance angle set at 3.5 msr. During the experiment, we optimized the spectrometer for the ^{24}Mg(^{3}He, t) channel to detect tritons corresponding to states in ^{24}Al. Nevertheless, other reaction products are inevitably produced and make it to the focal plane of the spectrometer. We can discriminate between the various ejectiles that are detected by comparing their energy loss characteristics through particle identification spectra measured by the drift chambers and the plastic scintillator detectors. The latter provided event trigger signals for the data acquisition. For such events, the position-sensitive drift chambers measure the position μ_{fp} and angle ϑ_{fp} of the ejectiles by reconstructing their ionized tracks, while the plastic scintillator detectors measure the energy deposited by these ejectiles. I briefly describe the operation of the drift chambers and the plastic scintillator detectors in the following sections.

2.1.1 The drift chambers

We used two multi-wire vertical drift chambers (VDCs) filled with a gas mixture of Ar and CO_2 (90%/10%), with 25 μm-thick mylar windows. As shown in the figure below, the VDCs are divided in an 'U-X' configuration that has 20 μm-thick cathode planes, with the U- and X-signal wire planes mounted at an angle of 50° and perpendicular to the scattering plane respectively [25]. The cathode planes are maintained at a high voltage of −3.5 kV for triton detection. Tritons that traverse through the drift chambers ionize atoms of the gaseous medium and produce electron-ion pairs, where the ionized electrons are drifted toward a signal wire that creates an electric field gradient. At sufficiently high energies, secondary ionization liberates additional electrons that eventually lead to an electron-avalanche [27]. We can use these electrical signals to re-construct the ionized track and extract directional information for tritons detected, as shown in Fig. 2.3.

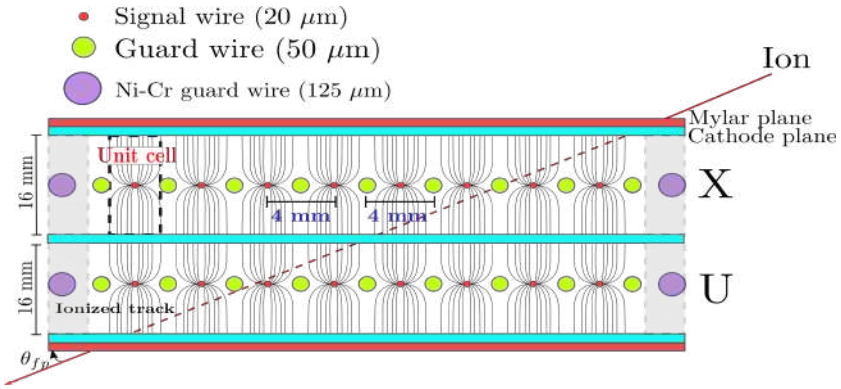

Figure 2.3: A cross-sectional top view of a multi-wire drift chamber (MWDC) where the X-wire plane is made up of 198 gold-plated tungsten signal wires interspersed with 199 field-shaping wires of the same material. The U-wire plane, mounted at angle of 50° relative to the scattering plane, is similarly made up of 143 signal wires and 144 guard wires [25]. The Ni-Cr guard wires at the periphery are used to reduce leakage currents by suppressing the spontaneous discharge of electrons.

2.1.2 The scintillator detectors

The ions that emerge from the VDC are incident on two rectangular plastic scintillator detectors that measure the energy of the ejectiles by converting its kinetic energy into detectable scintillation light, as illustrated in Fig. 2.4.

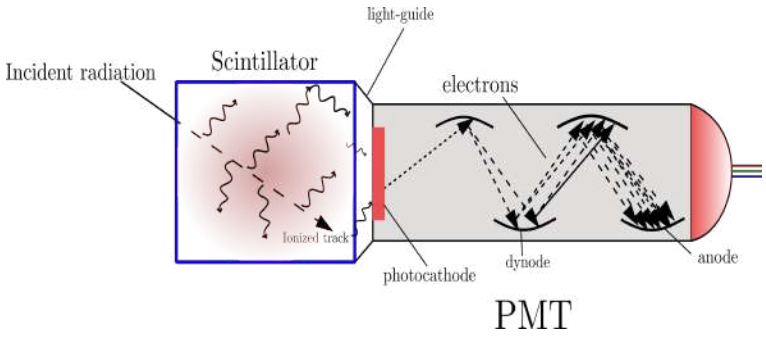

Figure 2.4: A scintillator detector coupled to a photomultiplier tube by a light-guide. The PMT converts the energy of incident radiation into a pulse through a series of dynodes that multiply the electrons ejected from the surface of the photocathode.

The ions deposit their energy in the active volume of the scintillator detector, exciting the atoms of the scintillation material. The excited atoms dissipate this excitation energy through electromagnetic radiation, with the photons guided onto a photocathode at the interface of the scintillator and the photomultiplier tube (PMT). Each photon has a finite probability of ejecting an electron from the surface of the photocathode which are then multiplied through a series of dynodes. These secondary electrons are then collected by the anode to form an output pulse whose amplitude is proportional to the energy of the incident radiation.

With the trigger signals generated by the scintillator detectors, coincidences between one drift chamber and one scintillator detector permit the identification of the reaction products from their energy loss characteristics provided by the scintillator ($E_{\mathrm{Scint2}} - \Delta E_{\mathrm{Scint1}}$) and their relative time-of-flight (*tof*) through the spectrometer. The *tof* refers to the time difference between the trigger signal and the next RF pulse from the cyclotron [26]. A picture of the drift chambers and the focal plane detectors with the accompanying cables are shown in Fig. 2.5. We can use the events registered by the focal plane detector to obtain the triton singles yield for the ^{24}Mg(^{3}He, t)^{24}Al reaction over a live time t^{run}, using

$$N^t = \frac{N_a}{t} \cdot X_{\mathrm{atoms}} \left(\frac{d\sigma}{d\Omega} \right) \cdot \Delta\Omega \cdot t^{\mathrm{run}} \cdot \epsilon_{fp}, \tag{2.2}$$

where $\frac{N_a}{t}$ is the number of incident projectiles per unit time, X_{atoms} is the areal number density of the target, $\left(\frac{d\sigma}{d\Omega}\right)$ is the reaction cross section, $\Delta\Omega$ is the acceptance solid angle of the spectrometer ($\sim$ 2.5 msr), and ϵ_{fp} is the intrinsic efficiency of the focal plane detector.

Figure 2.5: Position-sensitive drift chambers, with the plastic scintillator paddles at the focal plane of the $K = 600$ spectrometer. Figure taken from Ref. [28].

2.2 The silicon detector array

States above the proton separation energy S_p of the recoiling nucleus can decay via proton emission or γ-radiation. As mentioned previously, the decay amplitudes are described by the partial widths Γ_p and Γ_γ, with $\Gamma = \Gamma_p + \Gamma_\gamma$. We used a DSSSD array to detect such proton events, with the proton-triton $(p-t)$ coincidence yield for each unbound state

$$N^{tp} = \frac{N_a}{t} \cdot X_{\text{atoms}} \left(\frac{d\sigma}{d\Omega} \right) \cdot \Delta\Omega \cdot t^{\text{run}} \cdot \epsilon_{fp} \cdot B_p \cdot \epsilon_p, \tag{2.3}$$

where B_p is the proton branching ratio for a specific unbound state in ^{24}Al and ϵ_p is the proton detection efficiency. We can thus obtain the proton branching ratios of each state from Eqs. (2.2) and (2.3), so that

$$B_p = \frac{N^{tp}}{\epsilon_p N^t}. \tag{2.4}$$

A schematic of the array (called CAKE, Coincidence Array for $K = 600$ Experiments, [26]) used to detect the proton events is shown in Fig. 2.6. The CAKE array comprises five DSSSDs of the MMM design that are 400 μm thick with each detector covering ≈ 5 % of the solid angle [26, 29]. It has an energy resolution of ~ 100 keV covering an angular range of $\theta_{lab} = 115^\circ - 165^\circ$. An advantage of the CAKE array is offered by its efficiency and ring-sector design, as shown for one detector in Fig. 2.7.

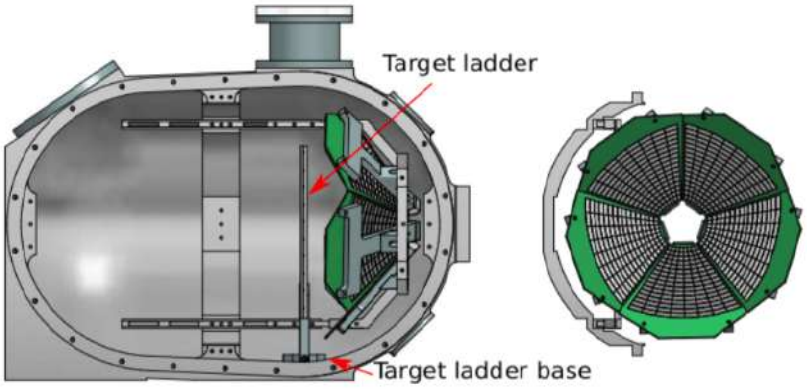

Figure 2.6: *Left*: The geometry of the CAKE array mounted upstream of the target ladder in the scattering chamber with the beam entering from the right. *Right*: The backward facing silicon detector array with a total efficiency ≈ 25 % [26].

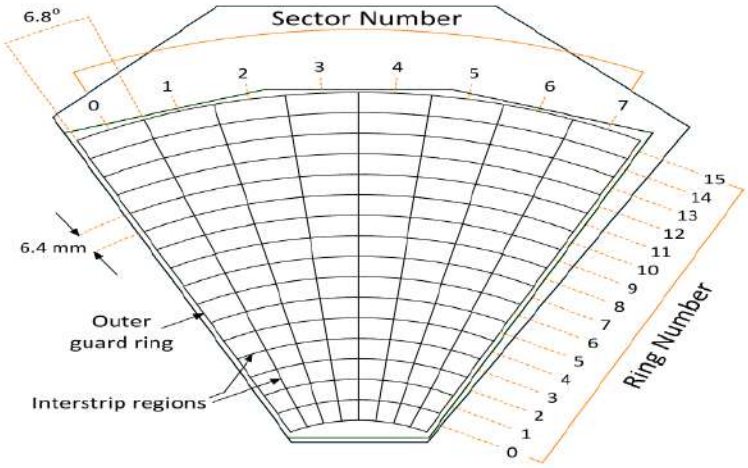

Figure 2.7: A schematic representation of a DSSSD of the MMM design with 16 ring channels on the junction side and 8 sector channels on the ohmic side. Figure taken from Ref. [26].

The junction and ohmic sides of the detectors can be leveraged to impose an energy condition so that the accidental coincidences with focal plane events are reduced, since the front and back energies should approximately be the same. This condition is based on the equal number of electron-hole pairs created in the front and back of the detectors and was imposed via software so that only events with

$$\left| \sum_{i=1}^{16} E_i - \sum_{j=1}^{8} E_j \right| < 300 \text{ keV}, \tag{2.5}$$

were accepted for the final analysis. In the following chapter I discuss more details on the analysis of the data obtained with these equipment.

Chapter 3

Data & Analysis

In this chapter I describe the analysis methods used to obtain the relative proton intensities of astrophysically important states in ^{24}Al. As mentioned previously, these states were produced using the ^{24}Mg(^{3}He,t)^{24}Al reaction at 50 MeV. We acquired around 60 hours of data with $\sim$10 pnA beam incident on target.

3.1 Targets used

A majority of the ^{24}Mg(^{3}He,t)^{24}Al data that were collected using a 200 μg/cm^2 thick MgF_2 target, evaporated on a 180 μg/cm^2 carbon backing. Additional data were also taken with a 700 μg/cm^2 thick ^{24}Mg target and a Li_2CO_3 target. The latter was used to mainly identify peaks from oxygen and carbon contamination in the MgF_2 targets, while the former was used for an initial energy calibration of the triton peaks. An empty target frame was also used to identify beam-induced background events.

3.2 Particle Identification

The predominant ^{24}Mg(^{3}He,d) and ^{24}Mg(^{3}He,t) reaction channels excite states in ^{25,24}Al, respectively. We leveraged the large difference in the Q-values of these channels to discriminate between the triton and deuteron ejectiles observed at the focal plane [30]. This is shown in Fig. 3.1, which plots the energy (ΔE) deposited in the scintillator detector versus the time-of-flight (*tof*) of the ejectiles through the spectrometer.

Although the spectrometer was optimized for the (^{3}He,t) channel, fluctuations in experimental conditions (predominantly from dispersion in the beam) become significant during different time periods of beam delivery. This is reflected by the measured properties of the reaction products $\{\Delta E_{scint}, tof, \mu\}$, μ being the focal plane position. Such systematic effects needed to be accounted for, in order to obtain position-aligned spectra for a large number of runs.

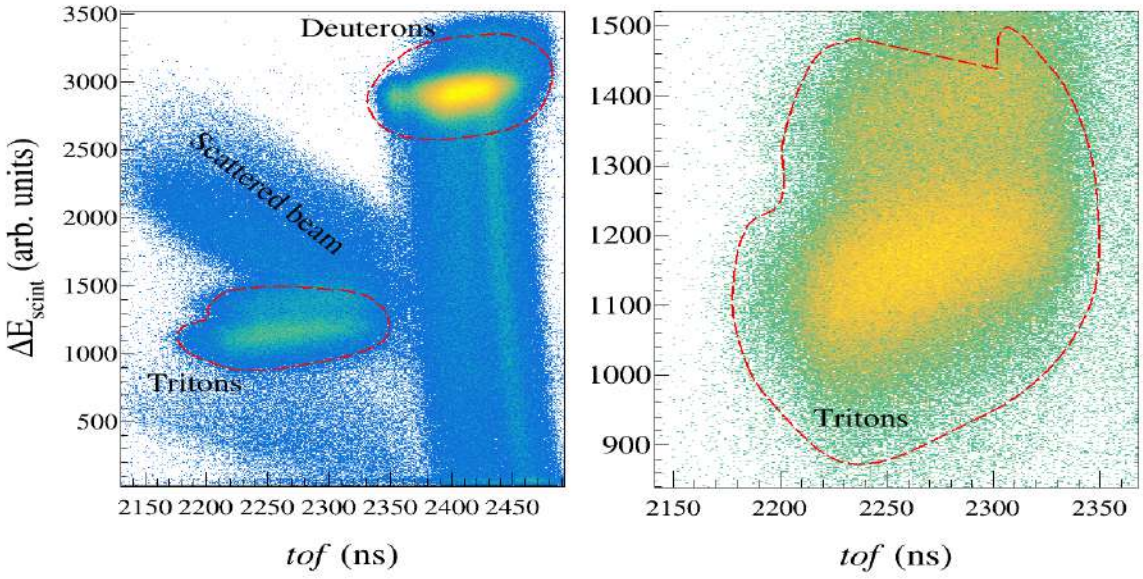

Figure 3.1: *Left panel*: The particle identification (PID) spectrum for our entire data set, with the thinner MgF_2 target. The triton and deuteron groups are highlighted. *Right panel*: An enhanced view of the PID gate on the triton group, used for the final data analysis.

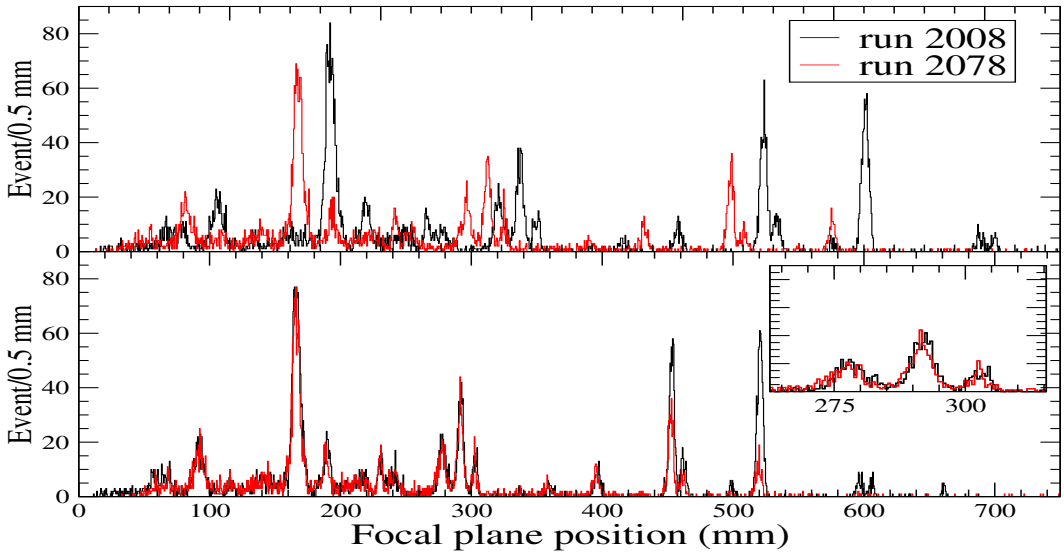

Figure 3.2: *Top*: The position spectra for two labeled 1 hour runs without correction. *Bottom*: Aligned position spectra for these runs, because of the offset correction. The inset accentuates the reasonably good alignment that was obtained with this simple correction.

Typically the focal plane position drift in the $K600$ spectrometer is characterized by a single offset parameter that aligns focal plane spectra from different runs. This is shown as an example in Fig. 3.2.

A further correction is required [25] to account for the scattering introduced by the 2° opening of the collimator that sets the angular acceptance of the spectrometer. We calibrated the measured focal plane angle ϑ_{fp} to obtain the scattering angle of the tritons ϑ_{fp}^{scat}, by implementing a set of conversion parameters in the sorting of the raw data. A successful calibration of ϑ_{fp} is characterized by the rectangular box in the 2D spectrum shown in Fig. 3.3. This completes the corrections required to produce position-aligned spectra for the entire data set [1].

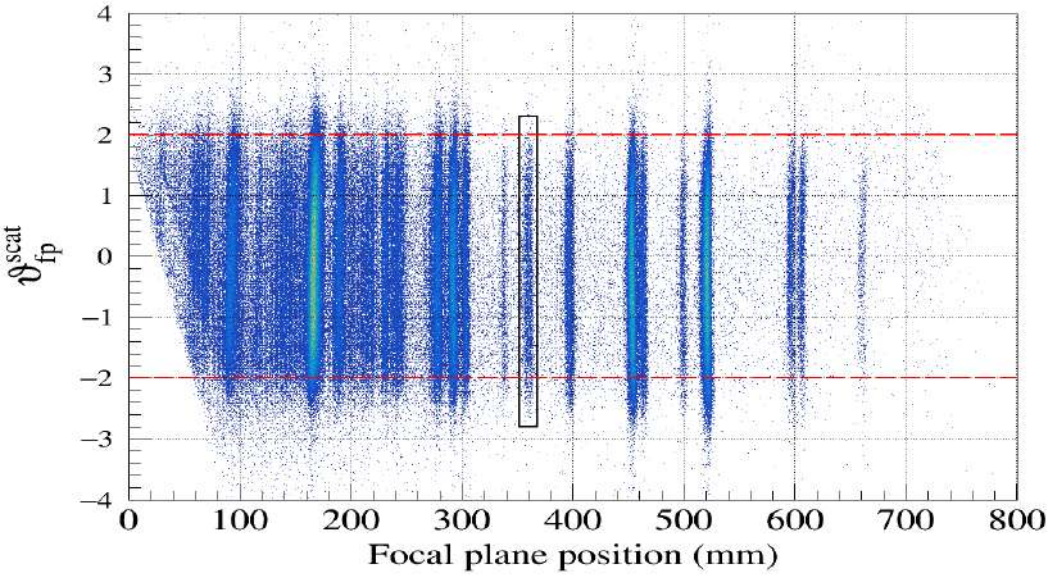

Figure 3.3: A 2D spectrum of the scattering angle ϑ_{fp}^{scat} versus focal plane position μ, measured by the drift chambers for the entire data set. The narrow vertical loci indicate the improved position resolution obtained through the imposed corrections. The black rectangle selects the astrophysically important state of interest in ^{24}Al at $\sim$ 2345 keV.

Finally, it may be noted that the calibration of the triton spectrum must account for energy straggling effects for the tritons that traverse through the target material. We therefore use a lineshape defined by a Gaussian distribution convoluted with a low-energy exponential tail [21] on a flat background to fit the triton peaks. A sample fit is shown in Fig. 3.4. Fits to the other peaks can be found in Appendix A. The triton spectrum for the entire data set, with labeled[2] peaks from states below the proton separation energy (S_p) shown in Fig. 3.5.

[1] As a test of our corrections, we note that the position resolution obtained for the entire data set is not appreciably worse than those from a single run.

[2] We defer a discussion on peaks above S_p to the next chapter.

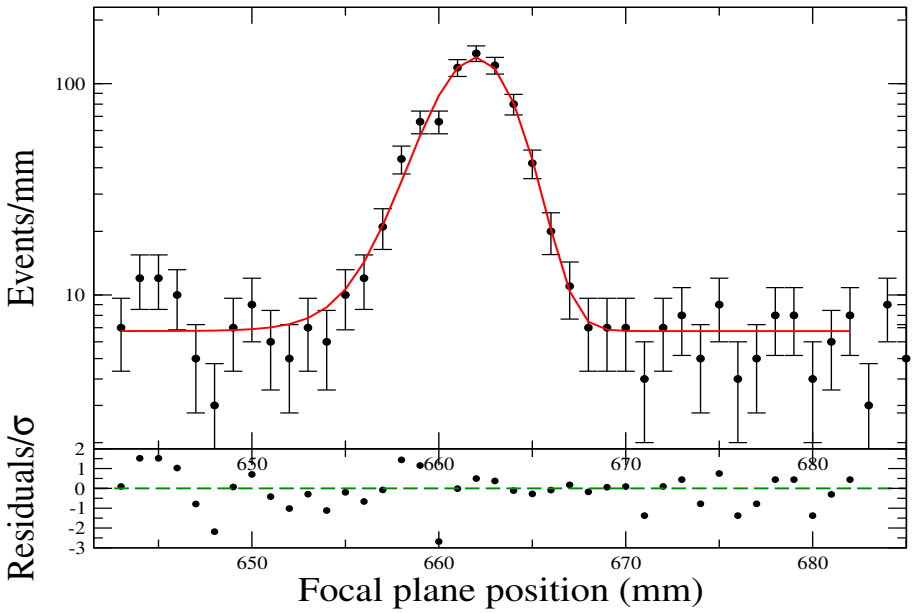

Figure 3.4: Sample triton lineshape fit to a triton peak, accounting for a low-energy tail because of straggling of the tritons. A description of the lineshape function can be found in Ref. [21].

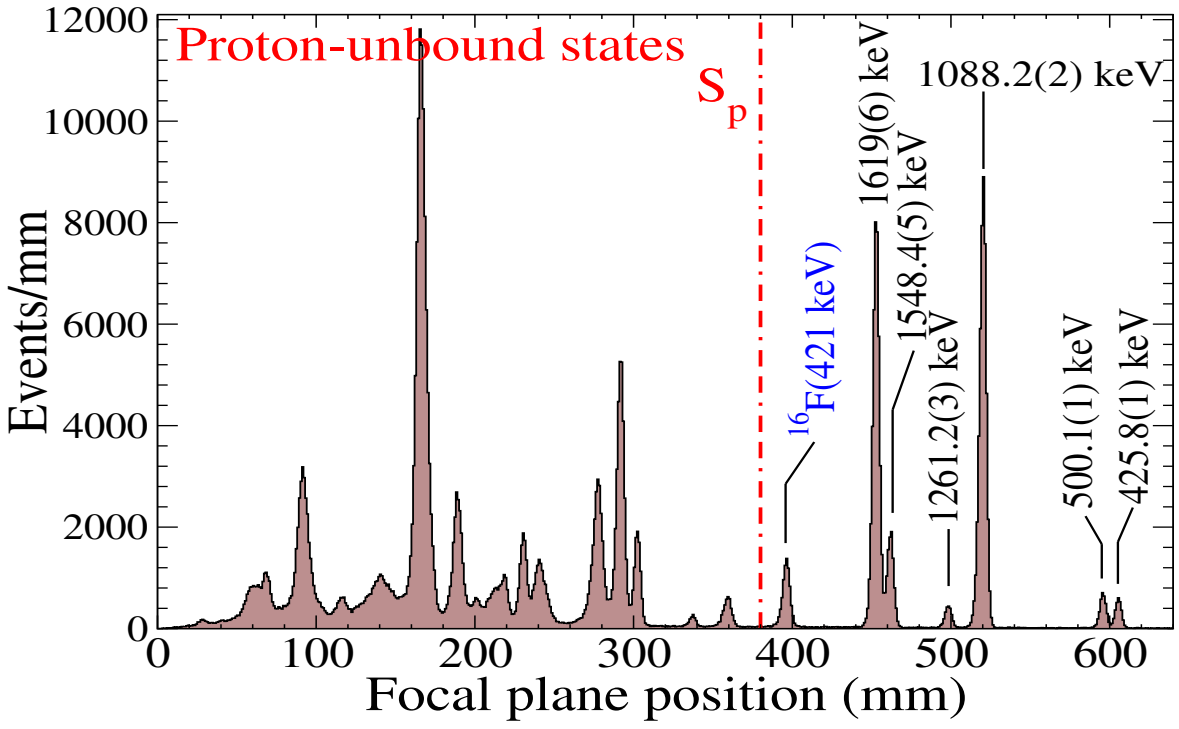

Figure 3.5: High-resolution triton spectrum obtained from our experiment. Only peaks below the proton separation energy are labeled here.

3.3 Energy calibration

The calibration of the triton spectrum is based on the conservation of the total energy E_T and total linear momentum $\overrightarrow{p}$ of the interacting nuclei, illustrated in Fig. 3.6.

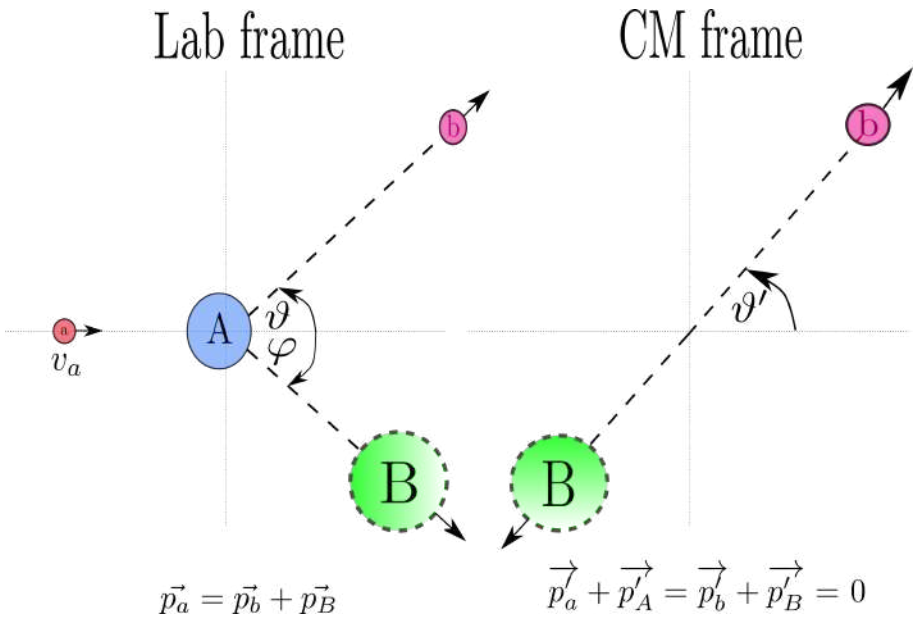

Figure 3.6: A pictorial representation of a binary reaction in the lab and the CM coordinate systems, where a and A represent the ^{3}He projectile and the ^{24}Mg target nucleus, and b and B represent the triton ejectile and ^{24}Al recoil, respectively.

An important equation that connects the total energy, mass and momentum of a particle is given by

$$E^2 = p^2c^2 + m^2c^4, \tag{3.1}$$

where the motion-dependent part is given by pc and the independent part is given by the rest energy of the particle mc^2 [31]. The kinematic relationships describing such two-body interactions yield the scattered energy of the light ejectile, provided that the total energy of the system, the rest mass of the interacting nuclei and the scattering angle of the ejectile are known. The following equations summarize the kinematic calculations carried out to obtain the energy of the ejectile, as described in Ref. [32].

On setting $c = 1$, Eq. (3.1) reduces to

$$E^2 = p^2 + m^2. \tag{3.2}$$

The Q-value for the reaction is defined by

$$Q = m_a + m_A - m_b - m_B, \tag{3.3}$$

which yields the threshold kinetic energy

$$W_{TH} = \frac{-Q}{2m_A}(m_a + m_A + m_b + m_B) \tag{3.4}$$

for the projectile to produce the outgoing particles. Using the minimum total energy of the projectile $E_a^{min} = W_{Th} + m_a$, we obtain

$$p_a^{min} = \left[\left(E_a^{min}\right)^2 - m_a^2\right]^{1/2} \tag{3.5}$$

for the minimum momentum of the projectile. We analyze the reaction in the center-of-mass coordinate system (i.e., $\sum_i \overrightarrow{p_i'} = 0$, shown in the right panel of Fig. 3.6) to simplify the calculation of the scattered energy of the light ejectile E_b', and use primed symbols to denote quantities in this system. The total energy of the system and momentum of the projectile is

$$E_T' = (m_a + m_A + 2m_A E_a)^{1/2}, \tag{3.6}$$

and

$$p_a' = p_A' = \frac{p_a m_A}{E_T'}. \tag{3.7}$$

With E_T' known, the total energy of the interacting nuclei in the entrance channel are given by

$$E_a' = \frac{m_a^2 + m_A E_a}{E_T'} \tag{3.8}$$

and

$$E_A' = \frac{m_A^2 + m_A E_A}{E_T'}, \tag{3.9}$$

whereas the total energy for the outgoing nuclei are given by

$$E_b' = \frac{E_T'^2 + m_b^2 - m_B^2}{2E_T'} \tag{3.10}$$

and

$$E_B' = \frac{E_T'^2 + m_B^2 - m_b^2}{2E_T'}. \tag{3.11}$$

With these relations for the interacting nuclei, with the light ejectile observed at θ_b, we can express the total energy of the ejectile in terms of the total energy E_T of the system and the masses of the interacting nuclei through [32]

$$E_b = \frac{1}{E_T^2 - p_a^2 \cos^2\theta_b} \left\{ E_T \left(m_A E_a + \frac{m_a^2 + m_A^2 + m_b^2 - m_B^2}{2} \right) \right.$$
$$\left. \pm\, p_a \cos\theta_b \left[\left(m_A E_a + \frac{m_a^2 + m_A^2 - m_b^2 + m_B^2}{2} \right)^2 - m_b^2 m_B^2 - p_a^2 m_b^2 \sin^2\theta_b \right]^{1/2} \right\}. \tag{3.12}$$

We next define a quantity α to clear up the ambiguity of the $\pm$ sign, so that

$$\alpha = \frac{p_a}{E_T} \left(1 + \frac{m_b^2 - m_B^2}{E_T'^2} \right) \left\{ \left[1 - \left(\frac{m_b + m_B}{E_T'} \right)^2 \right] \left[1 - \left(\frac{m_b - m_B}{E_T'} \right)^2 \right] \right\}^{-1/2}. \tag{3.13}$$

Then, for $\alpha > 1$ there exist two solutions for the scattering angle θ_b, and one solution for $\alpha < 1$, with the positive sign chosen for a physically meaningful solution. Having obtained this expression for the total energy of the scattered ejectile, the excitation energy of the recoiling nucleus can be obtained using energy conservation. Finally, the scattering angle of the ejectile in the center-of-mass system θ_b' can also be obtained through

$$\sin\theta_b' = \frac{p_b}{p_b'} \sin\theta_b \tag{3.14}$$

and

$$\cos\theta_b' = \frac{E_T}{E_T' p_b'} \left(p_b \cos\theta_b - \frac{p_a E_b}{E_T} \right). \tag{3.15}$$

We implemented the above kinematic equations in a C++ routine to carry out a momentum calibration of the tritons along the focal plane using the known excited states of ^{24}Al [23, 24, 33, 34]. Similarly, by shifting the input energies by one standard deviation ΔE_x one can estimate the associated momentum uncertainties Δp_t. Momentum values for isolated and strongly populated peaks μ_t were used to calibrate the triton spectrum through calibration coefficients obtained from a quadratic fit to (μ_t,p_t). The calibrated momentum values were then fed back into the kinematics code to yield the excitation energies E_x. The above procedure also takes into account the uncertainties in the ground state masses of the interacting nuclei. Adding all these contributions in quadrature then yields the total uncertainties for the extracted excitation energies. Fig. 3.7 compares the excitation energies obtained in this work to previously reported values. Evidently, a reasonable agreement is obtained with previous measurements. Further discussions are presented in the next chapter.

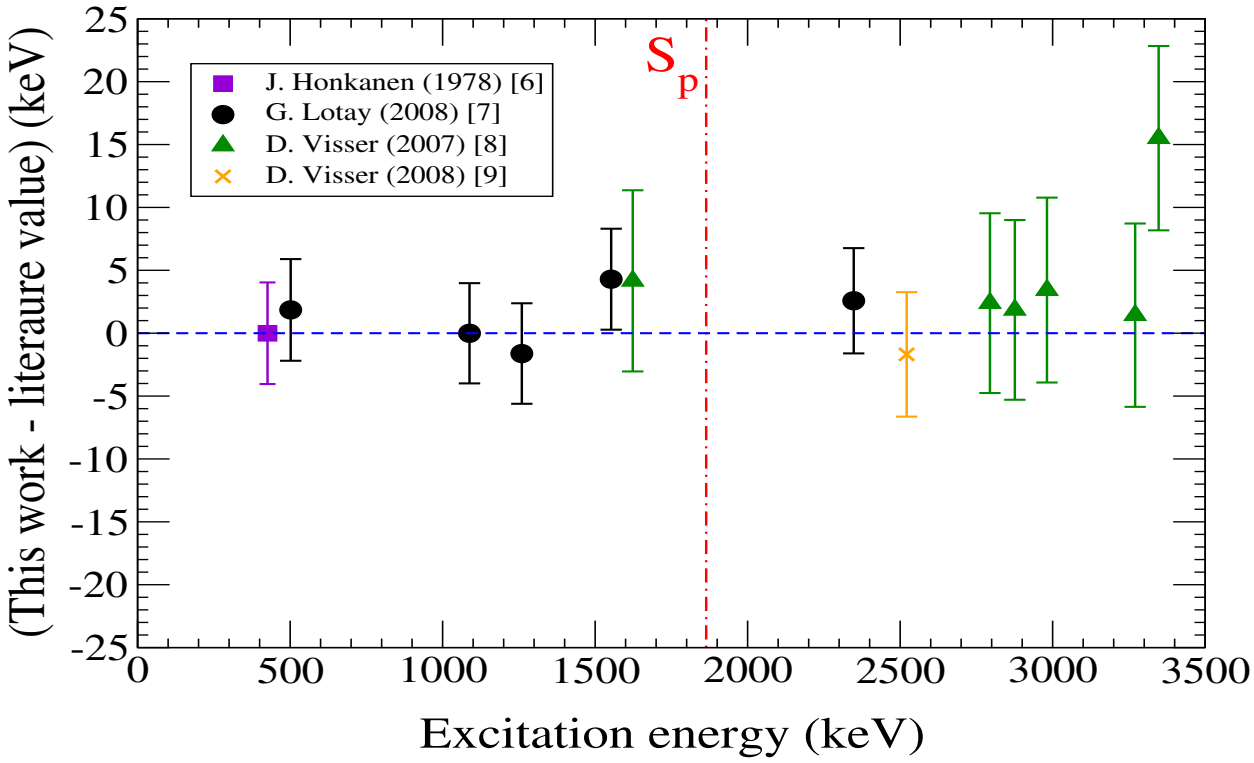

Figure 3.7: ^{24}Al excitation energies obtained in this work, relative to the values reported in the literature [23, 24, 33, 34]. We use $S_p = 1864$ keV, from measured atomic masses [35].

3.4 Coincidence analysis

In the following sections I briefly describe the analysis methods used to obtain proton-triton coincidence data, using the CAKE Si detector array.

3.4.1 Energy calibration of CAKE

Prior to beam acquisition, we used a ^{226}Ra source to calibrate each ADC channel of the CAKE array by identifying the α peaks from ^{226}Ra decay [36–38], shown in Fig. 3.8. We obtained the peak centroids $C(i)$ in the raw spectra for each ADC channel with a C++ program that uses the TSpectrum class of ROOT. The relationship between the uncalibrated (i.e., ADC value C) and the calibrated spectra was assumed to be in the linear form

$$E_\alpha(i) = a + bC(i), \tag{3.16}$$

where a and b are the offset and gain coefficients respectively for each detector channel. These coefficients were determined through a χ^2 minimization of a straight line fit to the peak centroids using the TMinuit library in ROOT. The projected spectrum of the 2D calibrated channels was used to validate our energy calibration of the CAKE array, with the identified α groups clearly resolved, as shown in Fig. 3.9.

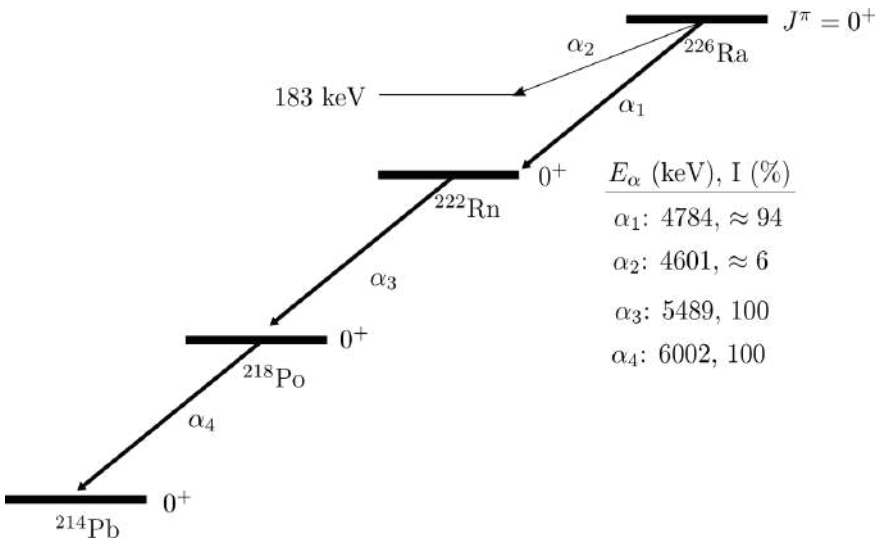

Figure 3.8: α decay chain for the ^{226}Ra source.

From this assessment, we can be confident that the MMM detectors were calibrated well enough to add the spectra from each MMM detector. The individual and summed spectra are shown in Fig. 3.10. It was also evident, after performing these energy calibrations, that the five MMM detectors were counting at roughly the same rate (see Table. 3.1).

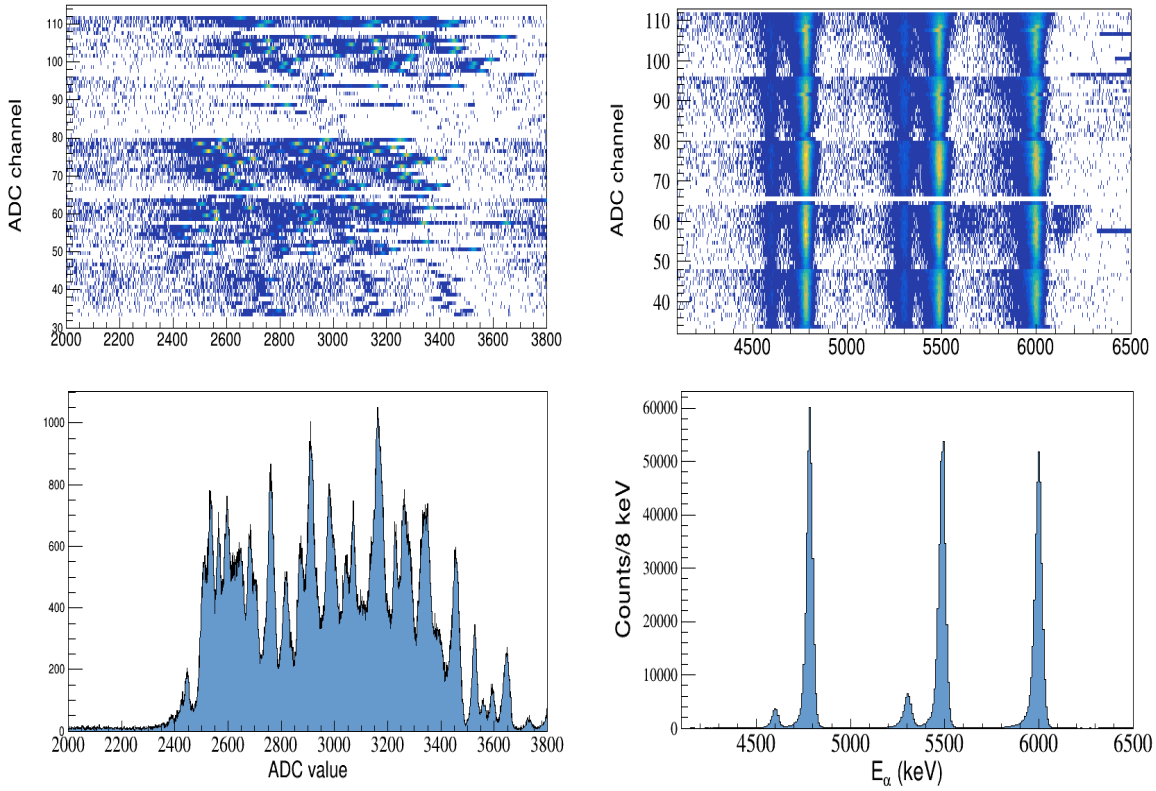

Figure 3.9: *Left panel*: Uncalibrated ring and sector channels of CAKE for the ^{226}Ra source data. *Right panel*: Energy-aligned spectra obtained after the calibrations were performed.

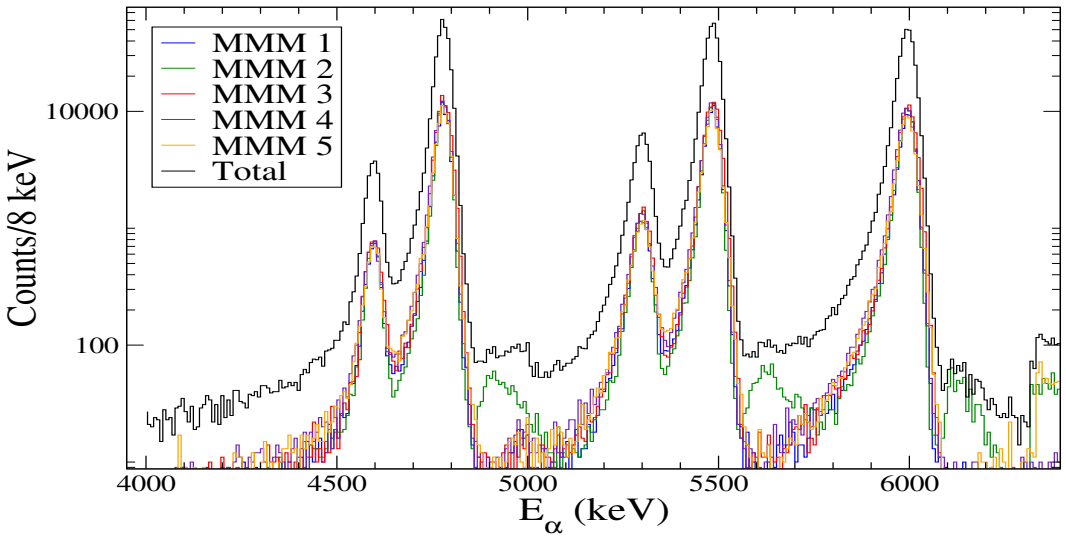

Figure 3.10: The calibrated spectra for each MMM detector, compared with the gain-matched spectrum of the total CAKE array.

Table 3.1: Areas obtained from a fit to the α peak around 6000 keV for each MMM detector and its contribution to the gain-matched spectrum of the total CAKE array.

MMM	Area (ΔA)	Contribution (%)
1	57243 $\pm$ 244	18.23 $\pm$ 0.08
2	59318 $\pm$ 247	18.90 $\pm$ 0.09
3	72285 $\pm$ 275	23.03 $\pm$ 0.10
4	67345 $\pm$ 266	21.45 $\pm$ 0.09
5	58530 $\pm$ 250	18.64 $\pm$ 0.09

3.4.2 Timing characteristics of CAKE

In order to obtain true coincidence data, with minimal random coincidences, the distribution of the values of the TDC channels of CAKE must be centered around zero. This permits the use of a narrow time gate for final data analysis. However, this is clearly not the case, as shown in Fig. 3.11.

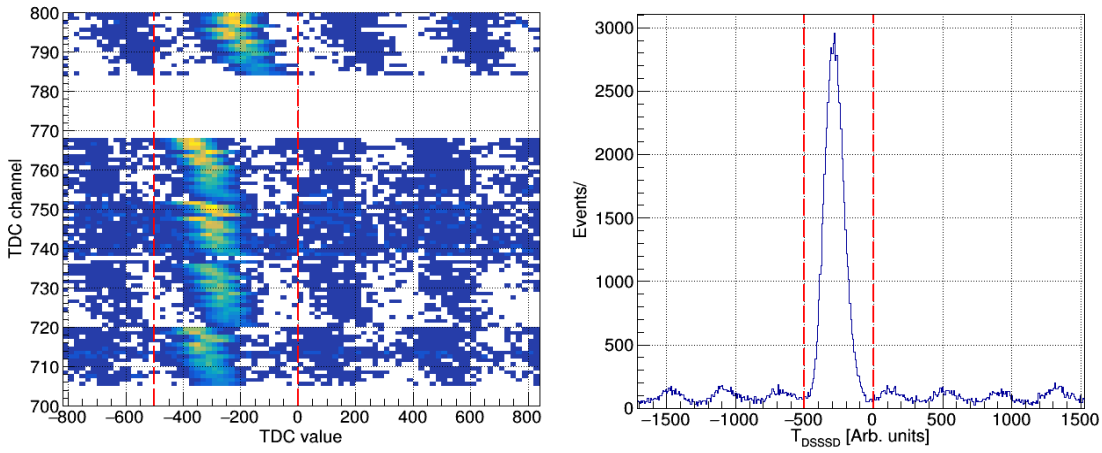

Figure 3.11: *Left panel*: The TDC channel versus its value for the experimental data with coincidences highlighted by the dashed vertical lines. *Right panel*: The timing distribution with a FWHM $\approx$ 72 channels.

We therefore implemented a set of offset and gain coefficients for the TDC channels of CAKE in the sorting code to obtain a sharper timing signal that is centered around zero. As shown in Fig 3.12, the improved FWHM value for the timing distribution validates the corrective procedure. By taking all the above corrections into account, we obtain the $p-t$ coincidence data shown in Fig. 3.13. An overlay of the coincident calibrated triton spectrum with triton singles is shown in Fig. 3.14.

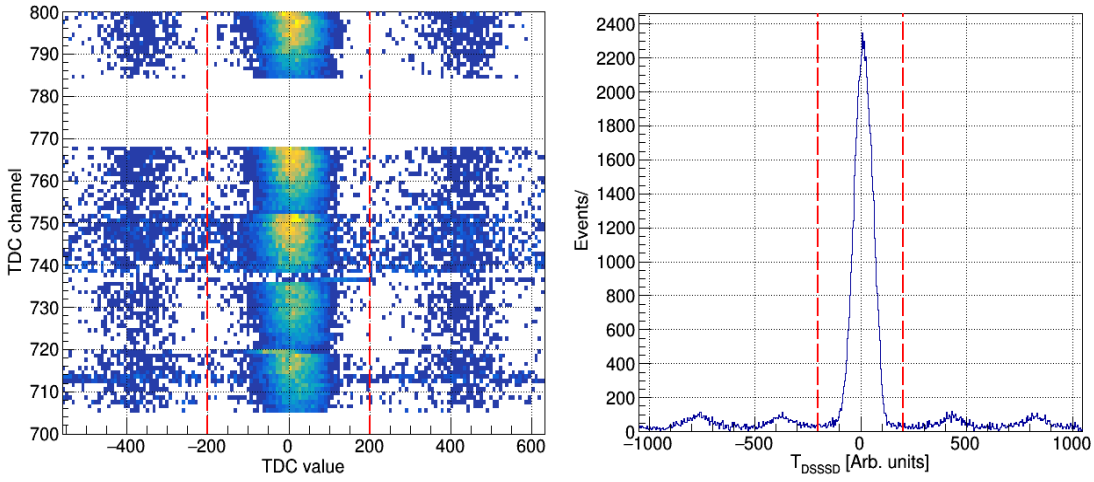

Figure 3.12: *Left panel*: TDC channels versus the corrected TDC values of the CAKE array. *Right panel*: The corresponding timing distribution that is centered around zero, with a FWHM $\approx$ 43 channels.

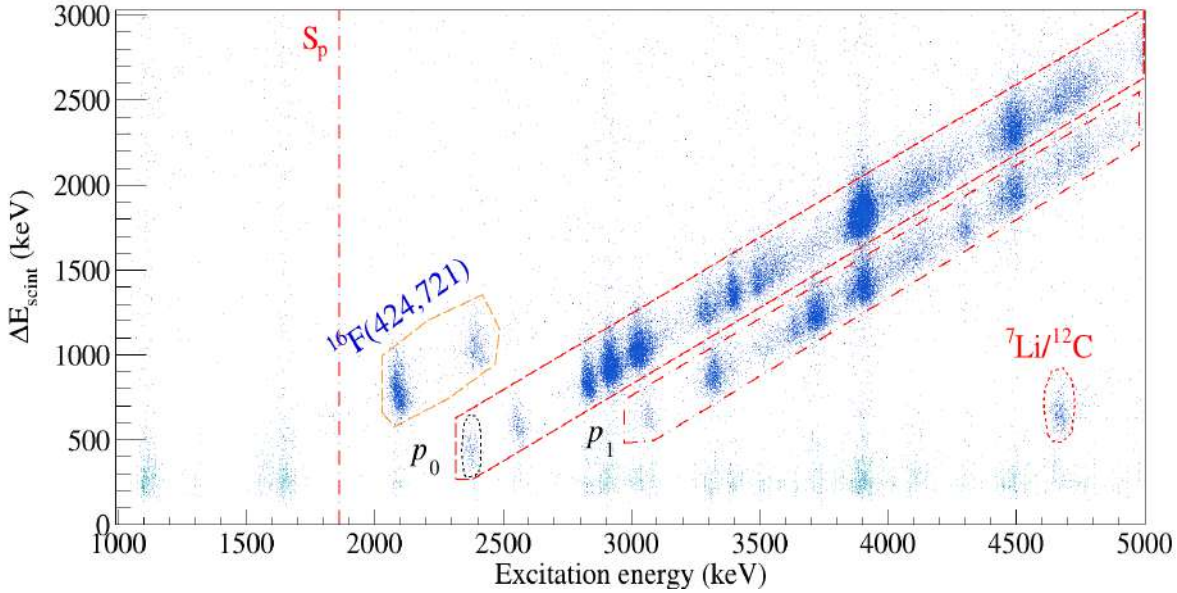

Figure 3.13: The $p-t$ coincidence data, with the proton decay modes of the ^{24}Al nucleus captured by the diagonal bands, where the upper (p_0) and lower (p_1) bands are from transitions to the ground and first excited states in ^{23}Mg, respectively. The ellipse around the p_0 proton group around 2400 keV highlights the lowest ^{23}Mg(p,γ) resonance.

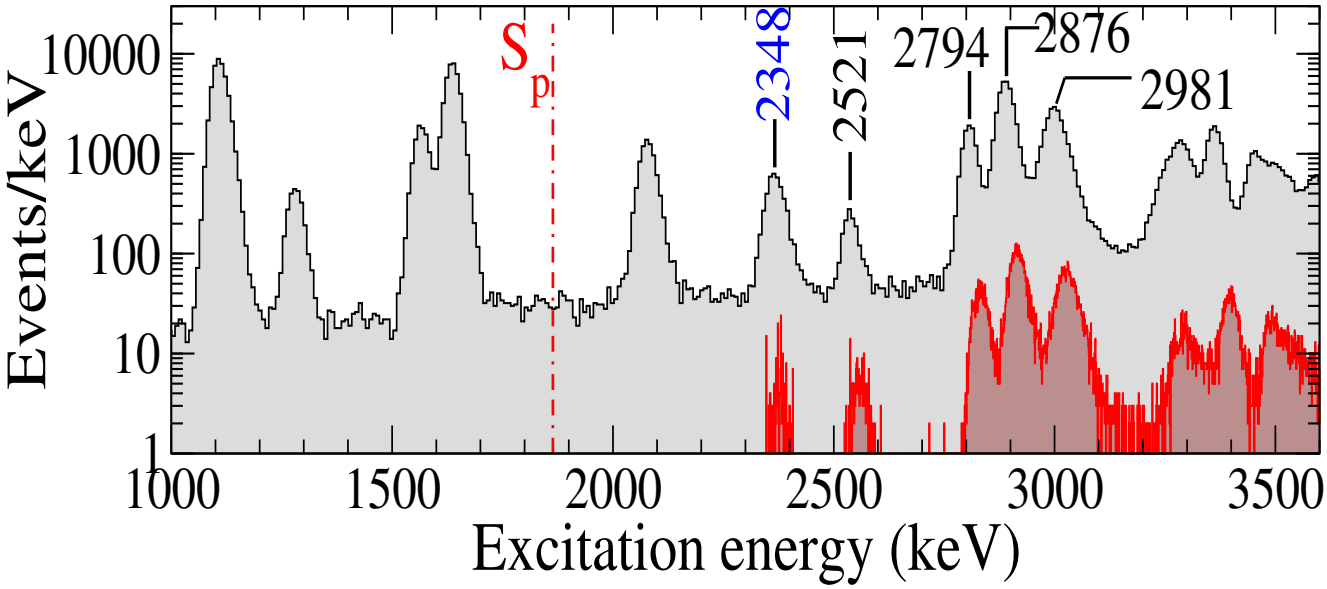

Figure 3.14: The singles triton energy spectrum of ^{24}Al, overlaid with coincidence data that correspond to the p_0 proton decay mode. We obtain $E_x = 2348(4)$ keV for the first state above $S_p = 1864$ keV.

Following the ^{24}Mg(^{3}He,t) reaction, the ^{24}Al recoils predominantly decay via proton emission in flight. I briefly discuss considerations of this aspect of the data analysis below.

3.4.3 Energies of the proton emitting recoils

As mentioned previously, we acquired data with the K600 spectrometer configured in 0° mode. The kinematic loci for both the tritons and the ^{24}Al recoils from the reaction are shown in Fig. 3.15. Assuming that only tritons emitted at an angular acceptance ±2° were detected at the focal plane, the reaction kinematics yield a ^{24}Al recoil energy $E_R \approx 210$ keV, with an energy spread $\Delta E_R \sim 7$ keV. Such a small initial recoil energy simplifies our analysis, as this results in $\beta = v/c \approx 4 \times 10^{-3}$ and

$$\gamma = \frac{1}{\sqrt{1-\beta^2}} \approx 1.0, \tag{3.17}$$

for recoils corresponding to $E_x \approx 2348$ keV[3]. Although the relativistic corrections to our analysis were negligible as shown above, for completeness, we performed an energy loss correction for the recoils. Because the ^{24}Al recoils lose energy through interactions with MgF_2 target atoms prior to proton emission, we need to account for this energy loss to determine the average recoil energy at the time of proton emission. This was obtained using the stopping powers $\left(\frac{dE}{dx}\right)$ for the ^{24}Al within the MgF_2 target, obtained from SRIM [39, 40]. We used the MgF_2 target density ($\rho = 1.3196$ g/cm^3) to convert the 200 μg/cm^2 target thickness to ≈ 154 μm in dimensions of length. This thickness was divided into N infinitesimally thin slices of thickness $\Delta x = \frac{154}{N}$ μm, with $N = 10^6$.

[3]In fact, such small corrections were applicable to the data from all the ^{24}Al proton-unbound states described in this work.

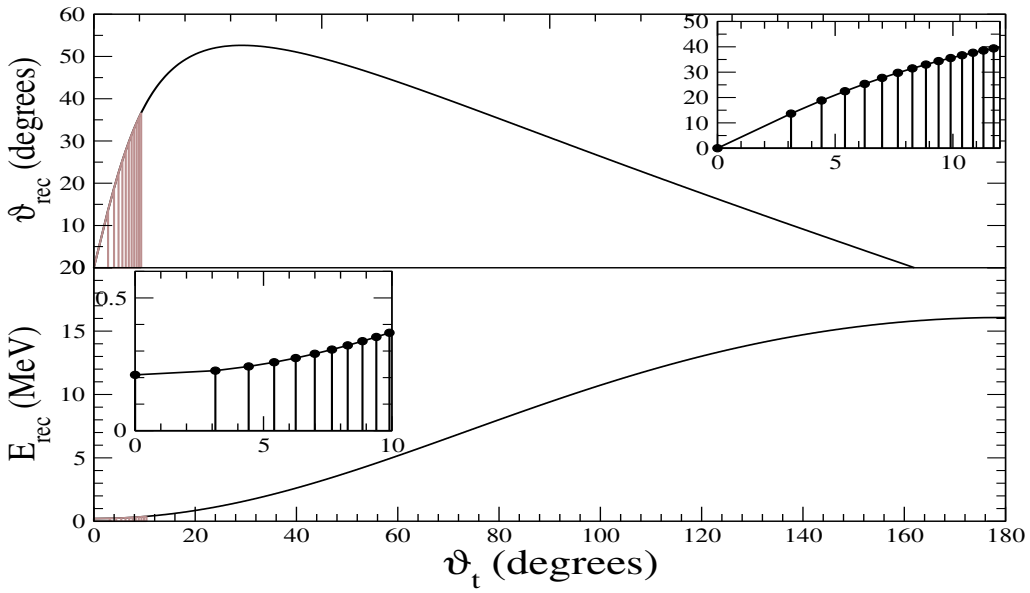

Figure 3.15: The angle and energy of ^{24}Al recoils for a range of triton angles in the lab frame. The shaded region indicates these variables at forward angles, up to $\sim 10°$. The inset highlights this region.

Each ^{24}Al recoiling nucleus approaches the first slice with initial energy $E_R = 210$ keV. After traveling a linear distance Δx, the energy loss of the recoil is given by the product $\left(\frac{dE}{dx}\right)_{E_R} \Delta x$. This essentially yields the reduced energy of the recoil for the first slice $E^R_{\rm red}$, with $v_R \simeq \left(2E^R_{\rm red}/m\right)^{1/2}$, assumed to be a constant over the infinitesimal slice. We can use this velocity to approximate the time of travel over that particular slice, using $t = \Delta x/v_R$. The calculation is then repeated for the subsequent slice, with the initial energy of the recoil being the reduced energy obtained for the previous slice and so on. This was generalized for i slices so that

$$E^R_{\rm red} = E_R - \sum_i \left(\frac{dE}{dx}\right)_i \Delta x_i, \tag{3.18}$$

with the $\left(\frac{dE}{dx}\right)$ value for each slice obtained from a polynomial fit to stopping power data obtained from SRIM, over a range of energies from 100 keV to 2000 keV. A third order fit shows reasonable agreement with the SRIM results, on assuming a 10% relative uncertainty in the stopping powers. The coefficients obtained from this fit, shown in Fig. 3.16, allow an energy-loss determination for arbitrary recoil energies.

The infinitesimal nature of the slicing also allows one to safely assume that the stopping powers remain constant over each slice. We used estimates of the proton widths to obtain the lifetimes of individual states, using the relation, $\tau_p = \hbar/\Gamma_p$. Since the proton width for the lowest-unbound state in ^{24}Al is calculated to be $\Gamma_p = 185$ meV [20], that yields $\tau_p \approx 3$ fs. With the above equations implemented in a C++ program, we obtained a total energy loss $\Delta E_R \approx 0.03$ keV for this state, with $\tau_p = 3$ fs imposed as a condition on the incremented time intervals $\sum_i t_i$. This negligible correction showed that energy-loss effects were

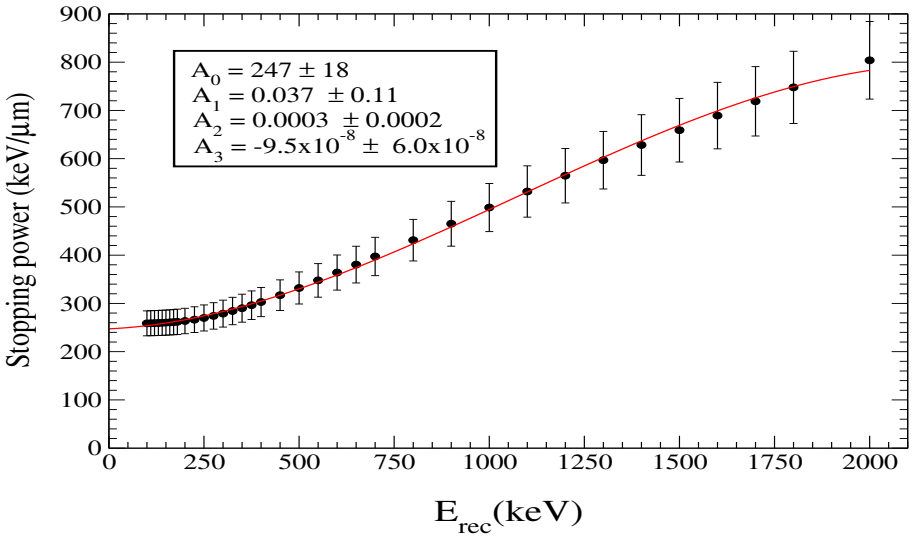

Figure 3.16: A third order polynomial fit to stopping powers versus recoil energies from SRIM, with both nuclear and electronic contributions summed. We used a conservative estimate of 10% relative uncertainty in the stopping powers from SRIM.

insignificant. The energy-loss corrections for the higher-lying states are much smaller, due to their shorter lifetimes. Details on the C++ program used to determine these corrections can be found in Appendix. B.1. For a ^{24}Al recoil that emits a proton leaving the residual ^{23}Mg nucleus in its ground state (i.e. a p_0 decay), the proton energy in the center of mass would be $E'_p = E_r$, the resonance energy. However, the energy in the lab frame depends on the velocity of the recoil. Since we already showed that the velocity of the recoils are small for this particular reaction, the energy of the protons in the lab can be approximated to

$$E_p \approx \left[\frac{\Delta\left(^{23}\mathrm{Mg}\right)}{\Delta\left(^{23}\mathrm{Mg}\right)+\Delta\left(^{1}\mathrm{H}\right)}\right] E'_p. \tag{3.19}$$

For the lowest-lying resonance at $E_r = 484$ keV, this yields $E_p \approx 463$ keV in the lab. In addition, the particle emission of recoils in flight require an additional relativistic correction for the angles at which the particles are detected. This is illustrated in Fig. 3.17. Resolving the momentum of the proton into its transverse $v_p^{\perp}$ and longitudinal $v_p^{\parallel}$ components

$$v'_p \sin\vartheta'_p = v_p \sin\vartheta_p \tag{3.20a}$$

$$v'_p \cos\vartheta'_p + \beta' = v_p \cos\vartheta_p, \tag{3.20b}$$

the relationship between ϑ'_p and ϑ_p is given by [41]

$$\tan\vartheta'_p = \frac{\sin\vartheta_p}{\gamma\left(\cos\vartheta_p - \beta'/\beta\right)}, \tag{3.21}$$

where $\beta' = \frac{v'}{c}$ in the center of mass system. For the purposes of our analysis since $\beta' \ll 1$ and γ is close to unity, we assume that $\vartheta'_p \simeq \vartheta_p$.

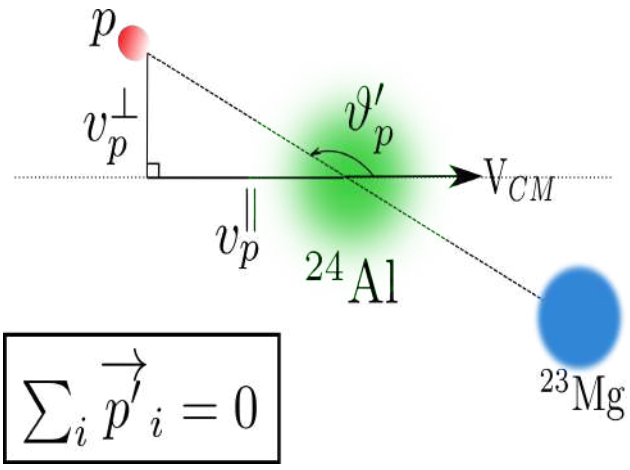

Figure 3.17: A pictorial representation of the in-flight proton decay of the recoil, moving with velocity $\beta' = V_{\mathrm{CM}}/c$.

3.5 Angular distribution of the protons

Since the total CAKE array subtends a fraction of the full solid angle, if the protons were emitted isotropically, one can obtain the proton branch from a ratio of $t - p$ coincidences to triton singles using the expression

$$B_p = \frac{1}{N_t} \sum_{i=1}^{16} \left(\frac{N_i^{tp}}{\epsilon_i} \right), \tag{3.22}$$

where N_i^{tp} represents the coincidences, N^t are the total registered triton singles and ϵ_i is the efficiency for each ring in CAKE. However, the protons carry orbital angular momentum. Assuming that the quantization axis is along the beam and ignoring higher order terms, the measured angular distributions of the protons are described by

$$W(\vartheta) = \sum_{k=0}^{2} A_k P_k(\cos\vartheta), \tag{3.23}$$

where the P_k's are Legendre polynomials. The A_k coefficients are parameters that describe the anisotropy of the proton angular distributions. An algebraic treatment [42] of the form of the expected angular distribution shows that the m-state population of a state characterized by $|J^\pi\rangle$ is greatly restricted for tritons accepted along the axis of cylindrical symmetry at $\sim 0°$. Taking these aspects into consideration, the ring-sector design of the CAKE array allows accurate angular distributions to be extracted from the coincidence data obtained.

Furthermore, since the DSSSD rings for CAKE cover the azimuthal angle φ in the interval $\varphi \in [0, 2\pi]$, we can obtain the proton branches from a fit to the measured angular distributions that incorporates the detection efficiency of each ring. Then the total branch is simply

$$B_p = \int_{-1}^{1} W(\vartheta) d(cos\vartheta). \tag{3.24}$$

As $W(\vartheta)$ is an even function, the only parameter that survives the integration in Eq. (3.24) is A_0. The proton branching ratio is therefore determined from the measured A_0.

3.5.1 Contamination in the triton spectrum

To obtain the proton branching ratios using the above procedure, it is essential that there is no contamination in our spectra. Inspection of the triton data obtained with the Li_2CO_3 target showed a peak at the same focal plane position as the triton peak that corresponds to the 2348 keV state in ^{24}Al. This is shown in Fig. 3.18, which overlays the triton singles spectrum from the Li_2CO_3 target with the spectrum obtained with the MgF_2 target. Peaks A', B' and C' are from ^{16}O(^{3}He,t) reactions and correspond to excited states in ^{16}F at 721 keV, 424 keV and the ground state respectively. Peak A in the ^{24}Mg(^{3}He,t) spectrum corresponds to the relevant excited state in ^{24}Al at 2348 keV. Since there are multiple contaminant peaks, their relative areas allow a correction for the contamination contribution to peak A.

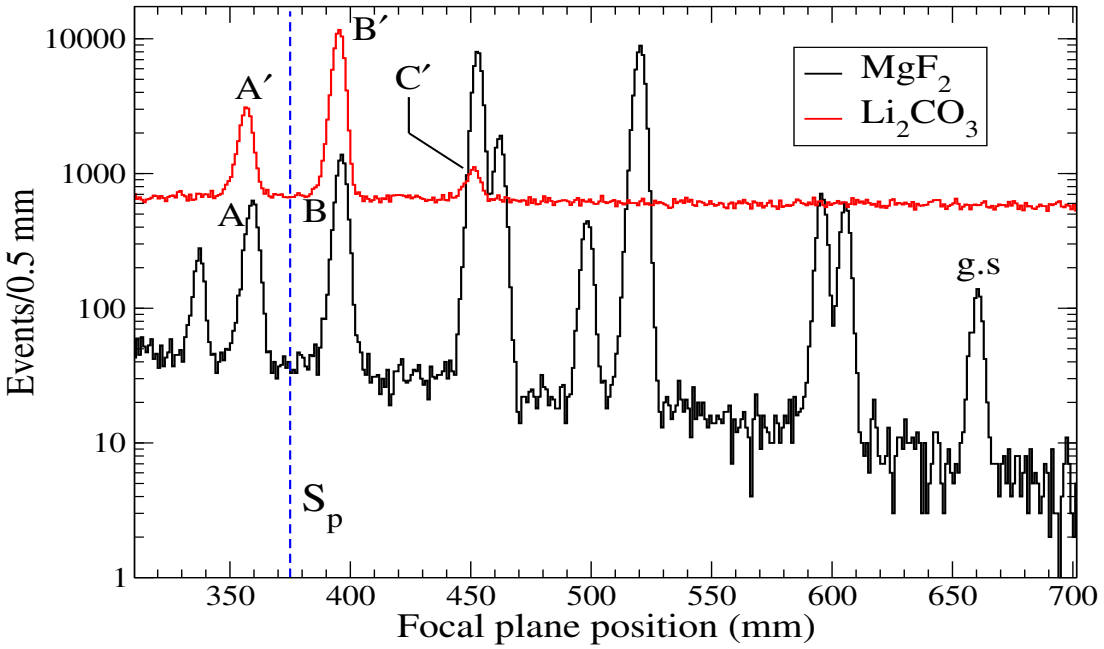

Figure 3.18: The triton spectra obtained for the MgF_2 and Li_2CO_3 targets. Triton peaks in the former are labeled by A and B. The contamination in the triton spectrum for the MgF_2 target are due to excited states in ^{16}F at 721 and 424 keV labeled by A' and B', with the ground state labeled by C' [43].

We define the ratio of the triton peak areas A' and B' for the Li_2CO_3 target as

$$\lambda' = \frac{A'_{363}}{B'_{398}}. \tag{3.25}$$

The triton peak area for the MgF_2 target with focal plane position ~ 363 mm includes triton peak contamination from the excited state in ^{16}F at 721 keV, which is given by $A_{\rm cont} = \lambda' B^{\rm peak}_{398}$. This allows one to obtain the contaminant subtracted triton peak area for the state of interest using

$$A^{\rm real} = A^{\rm peak}_{363} - A_{\rm cont}, \tag{3.26}$$

with the associated uncertainty $\Delta A^{\rm real}$ obtained by adding the uncertainties of the triton peak areas $\Delta A^{\rm peak}_{363}$ and $\Delta A_{\rm cont}$ in quadrature.

3.5.2 Detection efficiency of CAKE

A calculation of the detection efficiency of each ring gives the measured proton yield as a function of ϑ (including only the active elements of the detector for each ϑ). During the course of the experiment we observed that one ring and sector in MMM1 and MMM2 were not functional and yielded negligible events. This is shown in Fig. 3.19. We next used a GEANT4 Monte Carlo calculation [27] to obtain the efficiency of each active ring element. The simulations determined the detection efficiency

$$\epsilon_\vartheta = \frac{\text{events registered}}{\text{total number of events}}, \tag{3.27}$$

where the total number of events were emitted by an isotropic source placed at the center of the target. The simulations generated a sequence of random numbers for ϑ and φ distributed according to

$$\begin{aligned} \vartheta &= \cos^{-1}(2r_1 - 1) \\ \varphi &= 2\pi r_2, \end{aligned} \tag{3.28}$$

where r_1 and r_2 are random numbers uniformly distributed in $[0, 1]$. The above defined the polar and azimuthal directions for the protons, to yield an isotropic distribution for protons from the center of the target. For the dominant low-lying resonance, the source emitted around 10^6 monoenergetic protons with $E_p = 463$ keV. We imposed an energy condition ($E_p > 400$ keV) in the simulations, so that only events corresponding to proton energies in excess of this threshold energy were accepted. The accepted proton events are shown in Fig. 3.20.

The distributions of $\cos\vartheta$ and φ for the registered events from a sample simulation are shown in Fig. 3.21. We note that the flat nature of these distributions reflect the isotropy of the protons generated. We obtained a detection efficiency of $\sim 26\%$ for the total CAKE array, which is consistent with a previous measurement [26].

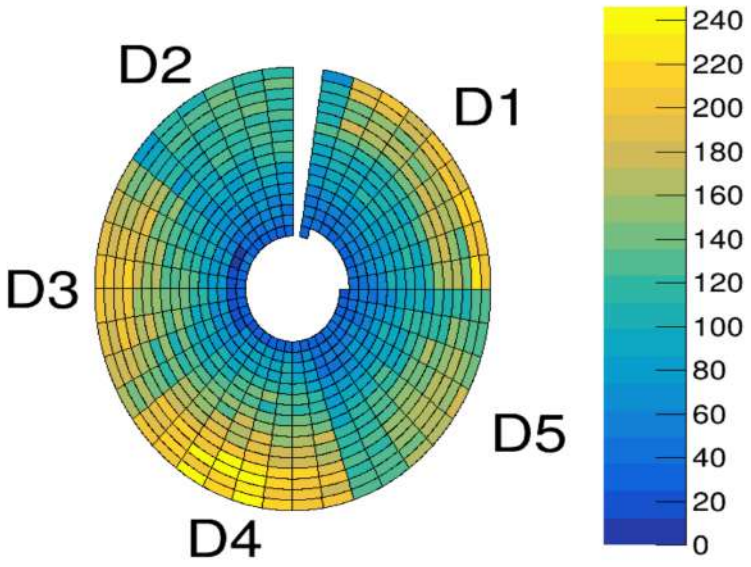

Figure 3.19: An upstream view of the experimental data for the CAKE array. Note that the CAKE array is not partitioned into the five MMM detectors in this visualization of the data.

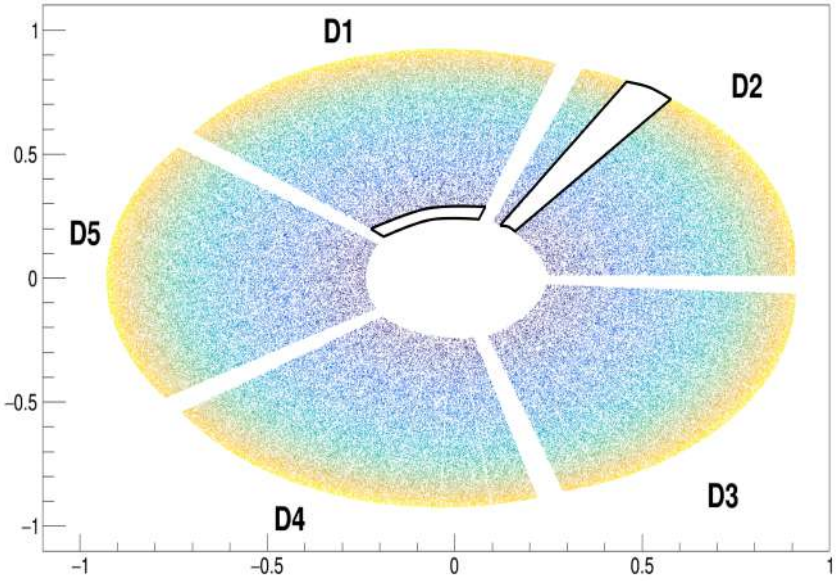

Figure 3.20: A downstream view of the GEANT4 simulated data of the CAKE array with the five MMM detectors partitioned, where the sectors in each MMM detector are clearly visible. The components of CAKE that were not active in the actual experiment were rendered inactive within the simulations. They are shown in this picture with dark boundaries.

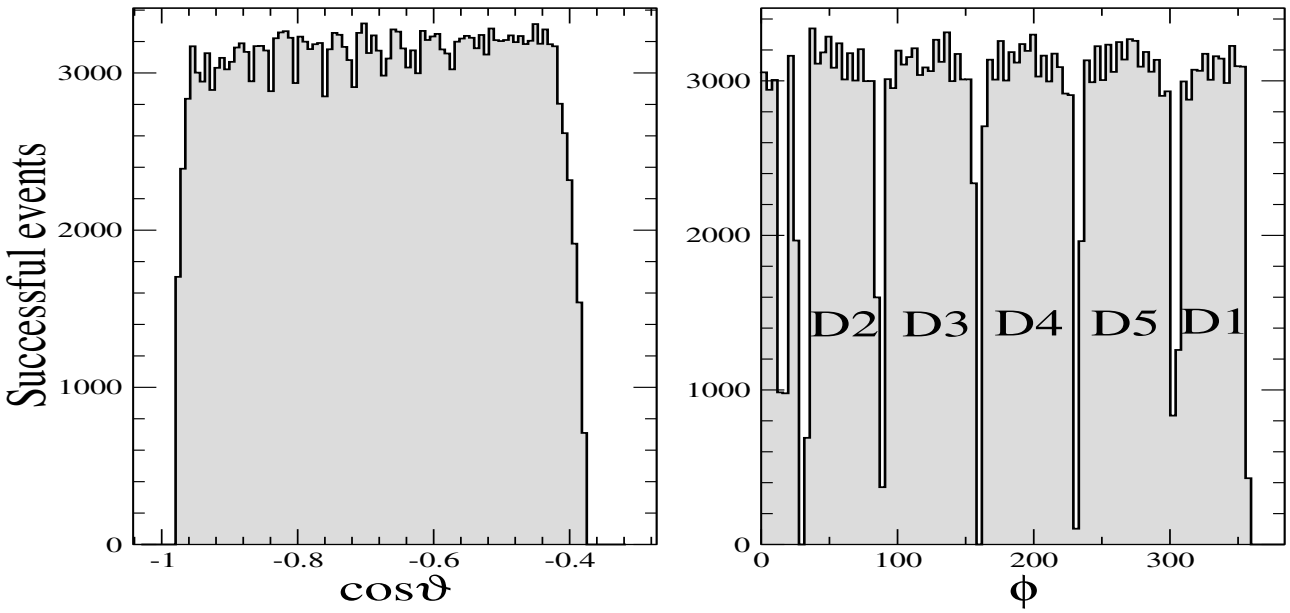

Figure 3.21: Isotropic polar (ϑ) and azimuthal (ϕ) distributions for the registered events, with the five activated detectors of the CAKE array labeled.

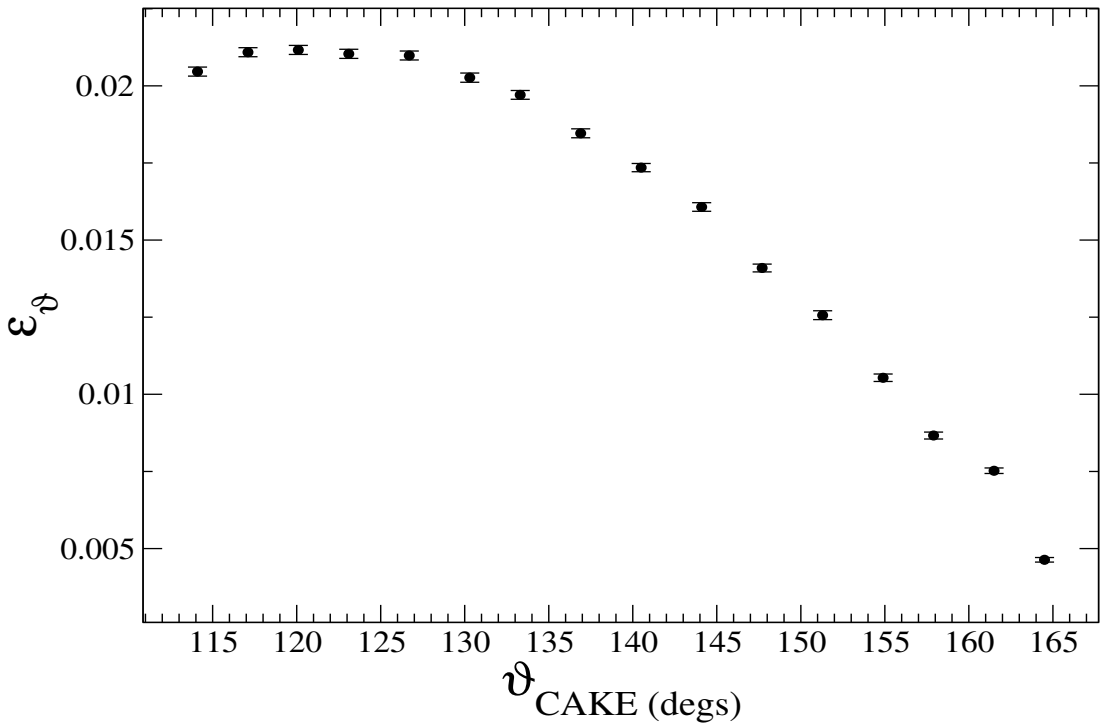

Figure 3.22: The detection efficiency of the rings at backward angles, obtained from a Monte Carlo simulation in GEANT4. Not surprisingly, the innermost ring at $\vartheta \simeq 165°$ has the lowest detection efficiency.

Finally, to correctly extract proton angular distributions from the coincidence data, it is crucial to map the proton intensities measured by each ring of CAKE to the appropriate ring detection efficiency. The latter was determined from events registered by each ring at angle ϑ, with the ring efficiencies shown in Fig. 3.22. The innermost ring at $\vartheta \simeq 165^\circ$ has the smallest surface area and thus expectedly has the lowest detection efficiency.

This concludes our discussion on the analysis methods used to obtain proton branching ratios for unbound states in ^{24}Al. In the next chapter I the discuss the results obtained in this work, and present a revised ^{23}Mg(p,γ) reaction rate.

Chapter 4

Results & Discussion

In this chapter I present the results obtained in this work, with emphasis placed on the first state above the proton separation energy in ^{24}Al. This is followed by an estimation of the total ^{23}Mg(p,γ) reaction rate at nova temperatures.

4.0.1 Level energies of ^{24}Al

With the focal plane position of the triton peaks carefully measured, the calibration of the triton momentum along the focal plane yield accurate excitation energies. The calibration procedure has already been discussed in Section 3.3. The final calibrated spectrum is shown in Fig. 4.1. The FWHMs of the peaks shown in this figure were $\leq$ 40 keV.

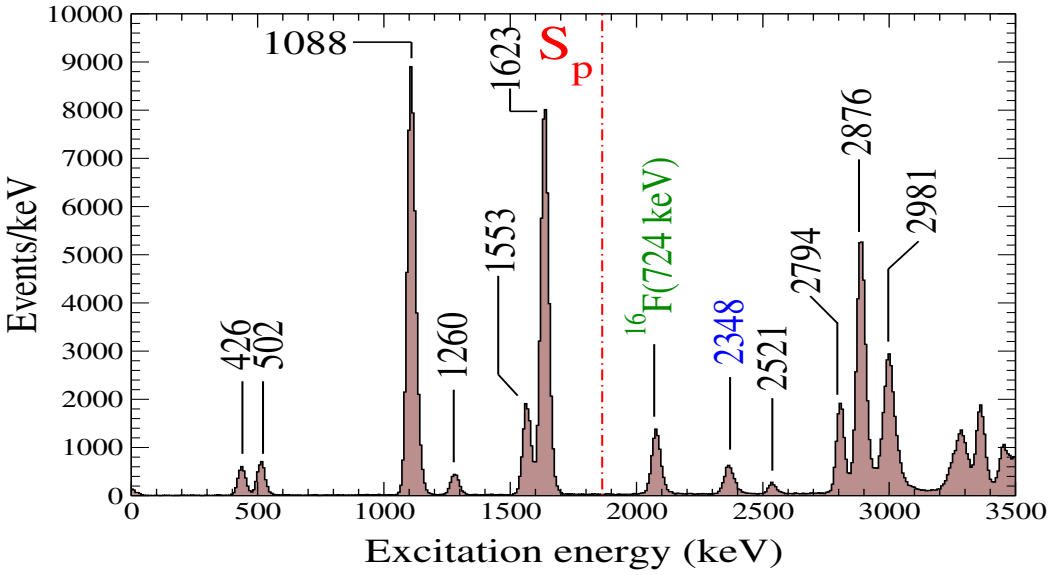

Figure 4.1: The calibrated spectrum of ^{24}Al up to $E_x \sim 3.5$ MeV. The prominent peaks in ^{24}Al and contamination from the 724 keV state in ^{16}F are labeled.

The average FWHM value for each peak obtained for the summed aligned-spectra for all runs was found to be comparable to that of a single run. We used $E_r = E_x - Q_{p\gamma}$ to determine the resonance energies corresponding to the excitation energies obtained in this work, where $Q_{p\gamma}$ is the Q-value of the ^{23}Mg(p,γ) reaction. We compare our extracted excitation energies and corresponding resonance energies to previous measurements in Table. 4.1.

We note that the difference between the resonance energies obtained from the present analysis and previously determined values are mainly due to the $\sim 6-8$ keV difference in the Q-values, as we rely on a more recent evaluation of the measured masses to determine $Q_{p\gamma}$ [35]. The calculated value for the resonance energy of the lowest-lying unbound state is in agreement with the adjusted values reported by Erikson *et. al* [9], which is also based on a similar $Q_{p\gamma}$-value.

4.1 Proton branching ratio measurements

The proton angular distribution of the lowest-lying resonance is shown in Fig. 4.2, and the distributions for the higher-lying resonances shown in Fig. 4.3. As previously discussed in Section 3.5, we can obtain the proton branching ratio from a Legendre polynomial fit to the measured angular distributions. We used a Gauss-Jordan minimization routine to perform this part of the analysis. The total width of each proton unbound state $\Gamma \propto N^t$, and it characterizes the probability of forming the state of interest in ^{24}Al. Its decay via proton emission is characterized by the partial width Γ_p, so that $\Gamma_p \propto N^{tp}$. Since the proportionality constants here are equal, we can express the proton branching ratio in terms of these widths through $B_p = \Gamma_p/\Gamma$ (see Eq. (3.22) in Section 3.5).

Our proton branches can then be used together with knowledge of the partial gamma widths to yield the resonance strength using $\omega\gamma = \omega\left(\frac{\Gamma_p}{\Gamma}\right)\Gamma_\gamma$. We relied on shell model calculations of the partial gamma widths ($\Gamma_\gamma^{\rm SM}$) of unbound states in ^{24}Al by Herndl [20] to obtain the resonance strengths, as these widths are difficult to measure directly. Following the prescription of Ref. [44], we assume a 50% uncertainty in the calculated $\Gamma_\gamma^{\rm SM}$. Our extracted values are shown in Table. 4.2, alongside shell-model calculated partial gamma widths and resonance strengths [19, 20]. These resonance strengths were then used to calculate the total ^{23}Mg(p,γ) reaction rate.

Table 4.1: The excitation energies and resonance energies of unbound states in ^{24}Al obtained here, compared with previous work.

Literature values											Present data	
Greenfield [18]		Kubono [19]		Herndl [20, 45]		Visser [23]		Lotay [24]	Zegers [46]	Erikson [9]	E_x	[b]E_r
E_x (keV)	E_r (keV)	E_x (keV)	E_r (keV)	E_x (keV)	E_r (keV)	E_x (keV)	E_r (keV)	E_x (keV)	E_x (keV)	E_r (keV)	(keV)	(keV)
1563(7)	...	1535(10)	...	1559(13)	...	1543(6)	...	1548.4(5)	1555(10)	...	1553(4)	...
1638(8)	...	1614(10)	...	1634(11)	...	1619(6)	...	1617.0(8)	1619(10)	...	1623(4)	...
2369(4)	506(4)	2328(10)	458(10)	2349(20)	478(20)	2346(6)	474(6)	2345.1(14)	2349(10)	[a]482.5(33),480(6)	2348(4)	484(4)
2546(7)	683(7)	2521(10)	651(10)	2534(13)	663(13)	2524(6)	652(6)	...	...	...	2521(4)	657(4)
2832(6)	969(6)	2787(10)	917(10)	2810(20)	939(20)	2792(6)	920(6)	...	2810(10)	...	2794(4)	930(4)
2920(23)	1057(20)	2876(10)	1006(10)	2900(20)	1029(20)	2874(6)	1002(6)	...	2890(10)	...	2876(4)	1012(4)

[a]Adjusted values of the resonance energies for the respective experiments of Refs. [23, 24].

[b]The excitation energy for the state was calibrated using the procedure described in Section. 3.3. The final uncertainty is obtained from adding the uncertainty contribution from $Q_{p\gamma}$ in quadrature.

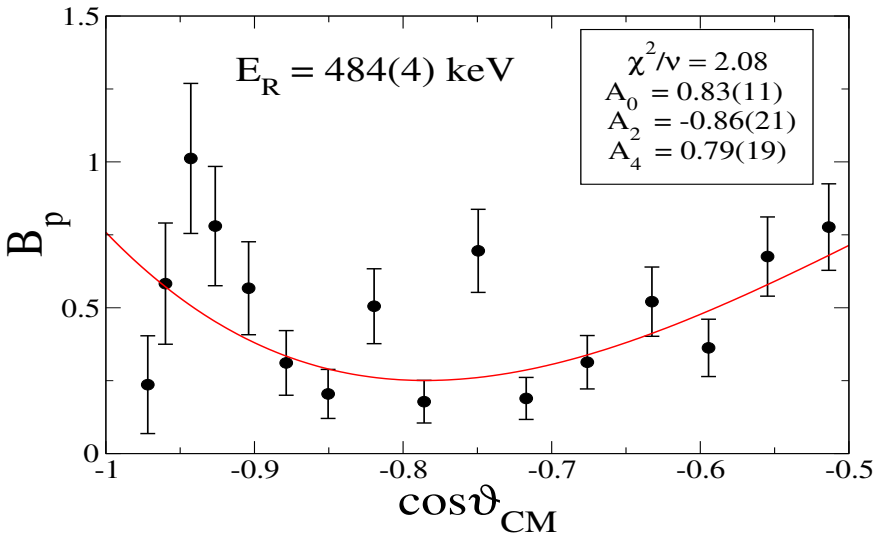

Figure 4.2: A Legendre polynomial fit to the angular distribution of the decaying protons that correspond to the first resonance in ^{24}Al. The anisotropy is characterized by the parameters A_2 and A_4. The uncertainties in the coefficients are extracted from the fitting routine, which is based on the Gauss-Jordan elimination technique and also takes into account off-diagonal terms in the covariance matrix.

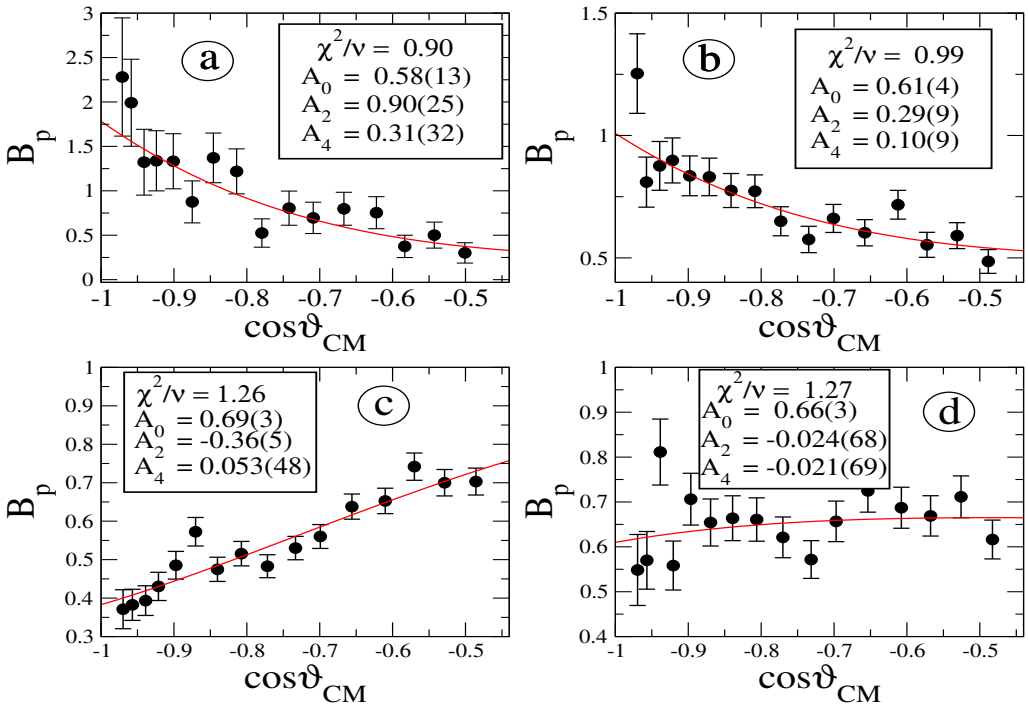

Figure 4.3: Legendre polynomial fits to the measured angular distributions of the decaying protons that correspond to the higher-lying resonances in ^{24}Al, labeled by **a**: $E_r = 657(4)$ keV, **b** $E_r = 930(4)$ keV, **c**: $E_r = 1012(4)$ keV and **d**: $E_r = 1117(4)$ keV.

Table 4.2: The proton branching ratios and resonance strengths obtained in this work, together with shell model calculated values of the partial gamma widths and resonance strengths.

Erikson. *et. al* [9]	Kubono. *et. al* [19]		Herndl. *et. al* [20]		Present data	
$\omega\gamma$ (meV)	Γ_γ (meV)[a]	$\omega\gamma$ (meV)	Γ_γ (meV)[b]	$\omega\gamma$ (meV)	Γ_p/Γ	$\omega\gamma$ (meV)[c]
38^{+21}_{-15}	47	26.8	33	25	0.83 ± 0.11	23.97 ± 12.39
...	160	128.7	53	58	0.58 ± 0.13	34.58 ± 18.95
...	13	11.4	83	52	0.61 ± 0.04	31.64 ± 15.96
...	> 26	16.3	14	12	0.69 ± 0.03	8.45 ± 4.24

[a]Adopted from the observed lifetimes for the analog states in ^{24}Na.

[b]Obtained using the OXBASH shell model calculation.

[c]Γ_γ taken from Ref. [20].

4.1.1 The ^{23}Mg(p,γ)^{24}Al stellar reaction rate

We used the RatesMC code [44] that is based on Monte Carlo techniques to estimate the total ^{23}Mg(p,γ) reaction rate in a statistically rigorous way. This approach allows an estimation of uncertainty bands in the reaction rates obtained. We already presented the formalism of the total reaction rate in Section 1.3, with the same approach employed in RatesMC to calculate the total reaction rate. This is summarized below.

For the nonresonant mechanism that dominates the total reaction rate at low temperatures, the total S-factor can be approximated by a polynomial

$$S(E) \approx S(0) + S'(0)E + \frac{1}{2}S''(0)E^2, \tag{4.1}$$

where the primed quantities refer to derivatives with respect to E. This yields the nonresonant reaction rate given by [44]

$$N_A\langle\sigma v\rangle_{nr} = \frac{4.339 \times 10^8}{Z_0 Z_1}\mu_{01} S_{\text{eff}} \exp^{-\tau} \tau^2, \tag{4.2}$$

where

$$\tau = 4.2487 \left(Z_0^2 Z_1^2 \mu_{01} \frac{1}{T_9}\right)^{1/3} \tag{4.3}$$

and

$$S_{\text{eff}} = S(0)\left[1 + \frac{5}{12\tau} + \frac{S'(0)}{S(0)}\left(E_0 + \frac{35}{36}kT\right) + \frac{1}{2}\frac{S''(0)}{S(0)}\left(E_0^2 + \frac{89}{36}E_0 kT\right)\right]. \tag{4.4}$$

In Eq. (4.2), μ_{01} refers to the reduced mass of the projectile and target in the reaction and N_A denotes the Avogadro constant. Furthermore, a cutoff factor $f_{\text{cutoff}} \approx e^{-T_9/T_9^{\text{cuttoff}}}$ that multiplies the reaction rate is introduced to account for temperatures at which the expansion of the S-factor becomes inaccurate [44]. In comparison, reaction rates for narrow resonances are obtained from the relation

$$N_A\langle\sigma v\rangle_r = \frac{1.5399\times10^{11}}{T_9^{3/2}}\mu^{3/2}\sum_i(\omega\gamma)_i e^{-11.605E_i/T_9}, \tag{4.5}$$

where the incoherent sum is over all resonance energies E_i and resonance strengths $(\omega\gamma)_i$. The total reaction rate is then given by the sum of the nonresonant and resonant reaction rates above.

In RatesMC, a probability density function is associated to each parameter that enters in the calculation of the total reaction rate. These include a Gaussian distribution for the resonance energy and lognormal distributions [44] for partial widths, resonance strengths and nonresonant S-factors. For the former distribution, negative random values are treated as subthreshold resonances in the Monte Carlo calculation. By drawing random samples from these distributions, one can obtain a set of randomly sampled reaction rates defined by a normalized lognormal distribution [44]

$$f(x) = \frac{1}{\sigma\sqrt{2\pi}}\frac{1}{x}\exp\left[-\frac{(\ln x-\mu)^2}{2\sigma^2}\right]. \tag{4.6}$$

The cumulative probability function (CDF) for the above is simply

$$F(x) = \int_{-\infty}^{x} f(x')dx'. \tag{4.7}$$

Using this method one can obtain a recommended reaction rate, given by the median value $x_{1/2}$. The uncertainty bands are determined by the 'low' and 'high' rates, coinciding with the 0.16 and 0.84 percentiles. This assures that the total reaction rate has a coverage probability of 68% [44].

We used our extracted resonance energies and resonance strengths as input to the RatesMC code to calculate the total ^{23}Mg(p,γ) reaction rate. Our adopted uncertainty in $\Gamma_\gamma^{\rm SM}$ is supported by a systematic comparison of partial widths [44]. A further description on the nuclear physics input used to compute the total reaction rate can be found in Ref. [47]. The output for the total reaction rate is shown in Fig. 4.4, with the contributions of the nonresonant (direct capture, DC) and resonant components to the total reaction rate shown in Fig. 4.5. Finally, we compare our revised estimate of the total ^{23}Mg(p,γ) reaction rate with the evaluation by Herndl [20], shown in Fig. 4.6.

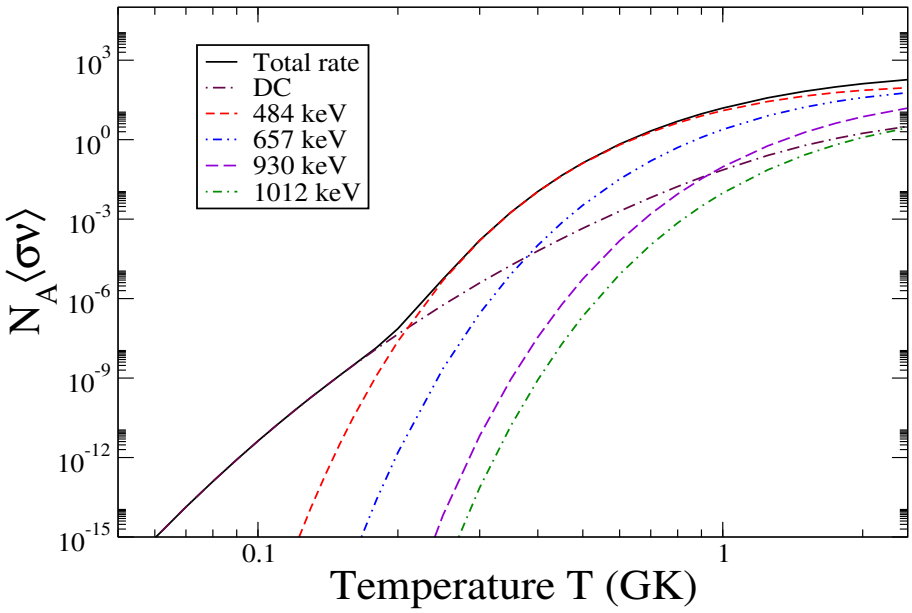

Figure 4.4: The total ^{23}Mg(p,γ) reaction rate corresponding to four low-lying resonances observed in this work, with the total S-factor for the nonresonant component (DC) adopted from Ref. [20].

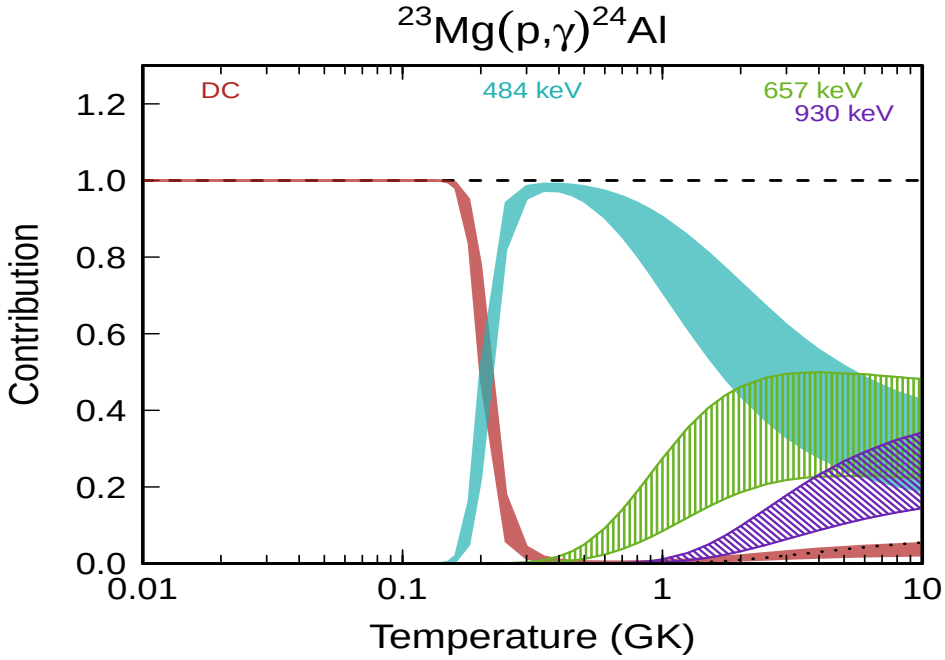

Figure 4.5: The contribution of the direct capture (DC) component and the low-lying resonances to the total ^{23}Mg(p,γ) reaction rate. The uncertainties of the various contributions to the total reaction rate are indicated by the bands.

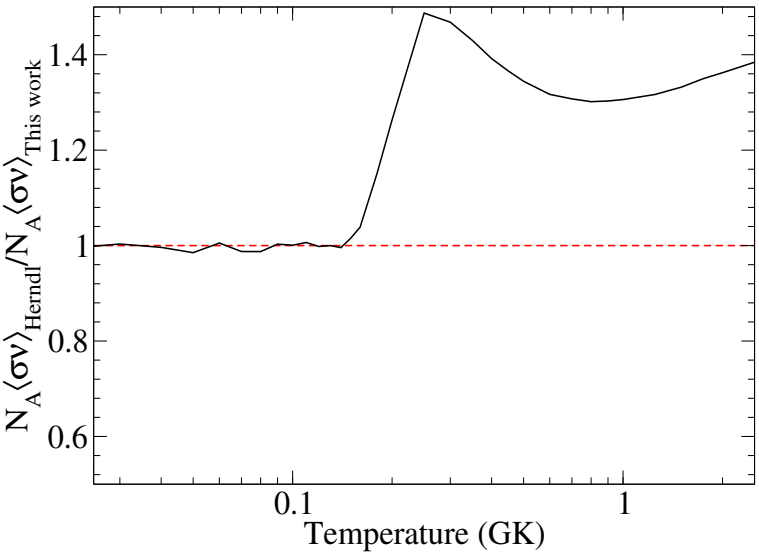

Figure 4.6: A comparison of the total ^{23}Mg(p,γ) reaction rate obtained in this work with a previous estimate by Herndl [20], over a range of temperatures from 0.05 GK to 2.5 GK.

This concludes our discussion of the results obtained in this work. We note that we obtain reasonable agreement with previous measurements [9, 20, 23]. This is the first direct measurement of relative proton branching ratios from ^{24}Al to estimate ^{23}Mg(p,γ) resonance strengths to astrophysically relevant states. Our extracted value for the resonance strength for the 3^+ state at 2348 keV is in agreement with the direct measurement by Erikson *et. al* [9]. However, the uncertainty in our value is dominated by the 50% relative uncertainty assumed for the calculated gamma width of this state.

4.2 Conclusions

This work focused on measurements of the proton branches for the unbound states in ^{24}Al. We obtain the excitation energy of the first proton-unbound $J^\pi = 3^+$ state in ^{24}Al to be $E_x = 2348(4)$ keV. Together with our measured proton branching ratio, this allows us to obtain the resonance strength of this dominant resonance in the astrophysically relevant ^{23}Mg$(p,\gamma)^{24}$Al reaction. Our extracted value of the resonance energy for this state is $E_r = 484(4)$ keV.

An analysis of the angular distribution of the decaying protons from the lowest-lying unbound state yields a proton branching ratio, $B_p = 83 \pm 11\%$. This proton branch and the shell model estimate of the partial gamma width of this state gives the resonance strength, $\omega\gamma = 24.0 \pm 12.4$ meV. We considered four resonances and the direct capture mechanism to obtain a revised total ^{23}Mg$(p,\gamma)^{24}$Al reaction rate. It is anticipated that our results will form part of a useful input to ONe nova models for stellar nucleosynthesis. Future measurements of the Γ_γ widths for these states will be useful in this regard.

Appendix A

Focal plane position centroids

A fit to the triton focal plane positions (μ_t) using the lineshape function previously described are shown below, with the resulting position centroids and areas collected in Table. A.1.

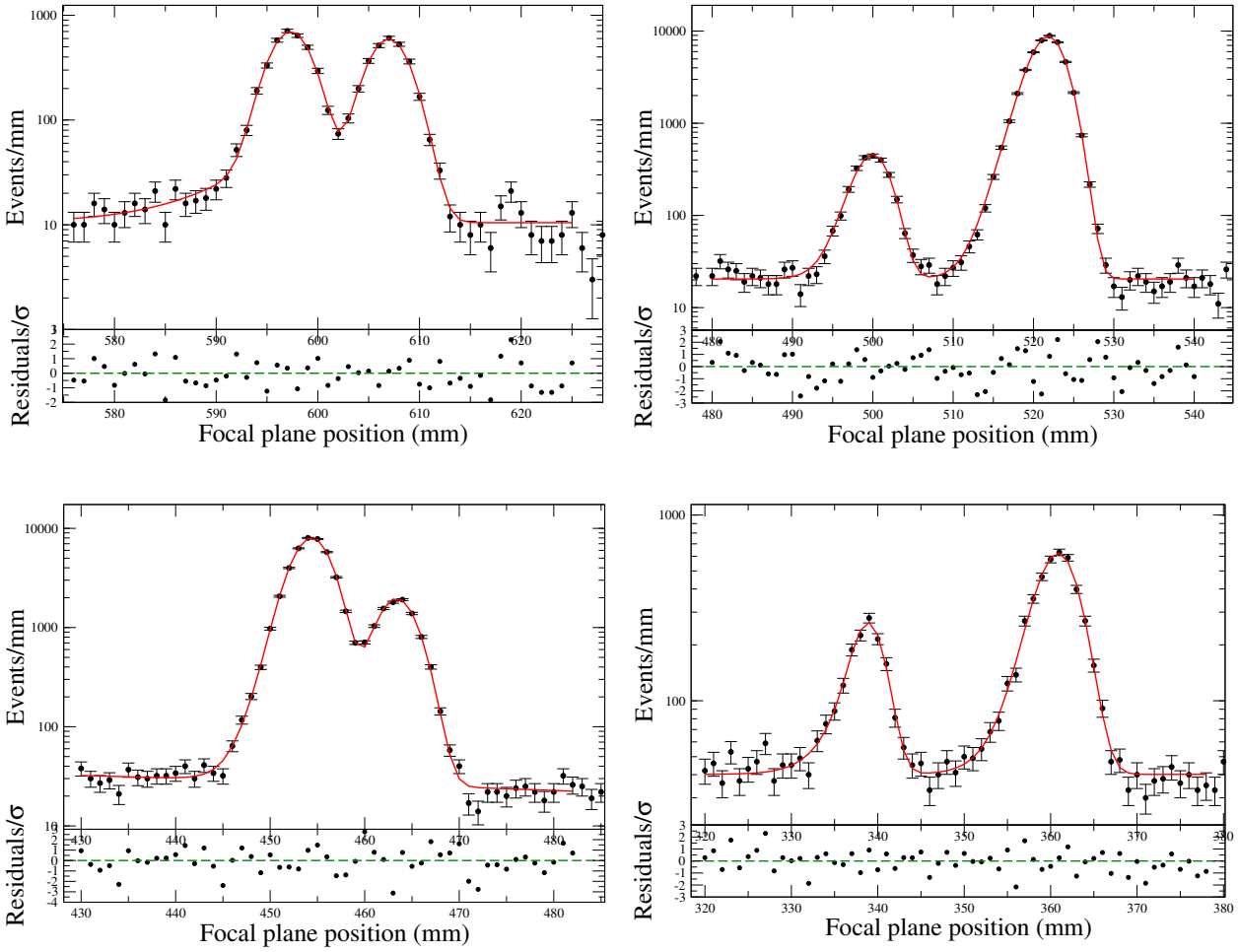

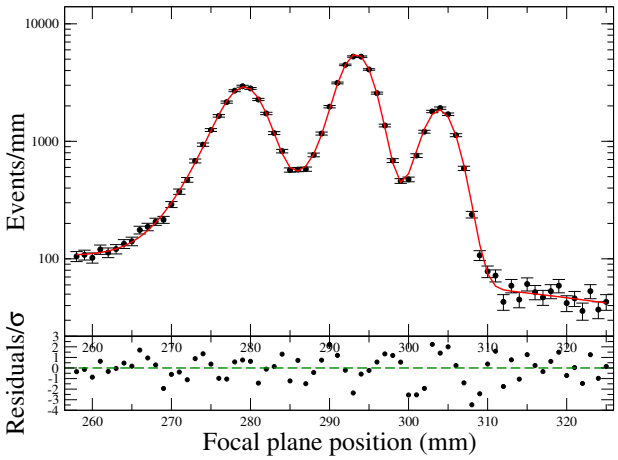
Events/mm
Residuals/σ
Focal plane position (mm)

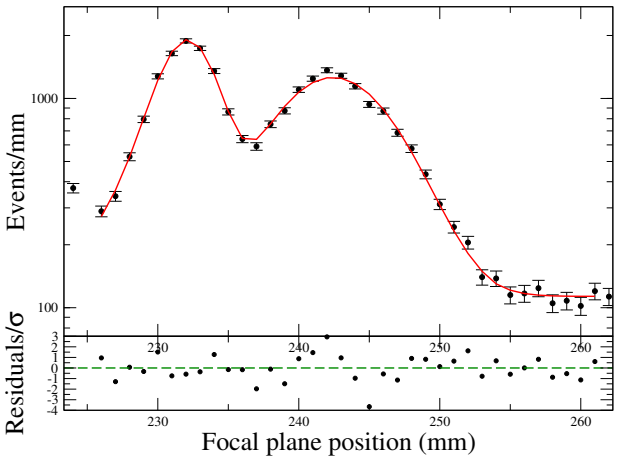
Events/mm
Residuals/σ
Focal plane position (mm)

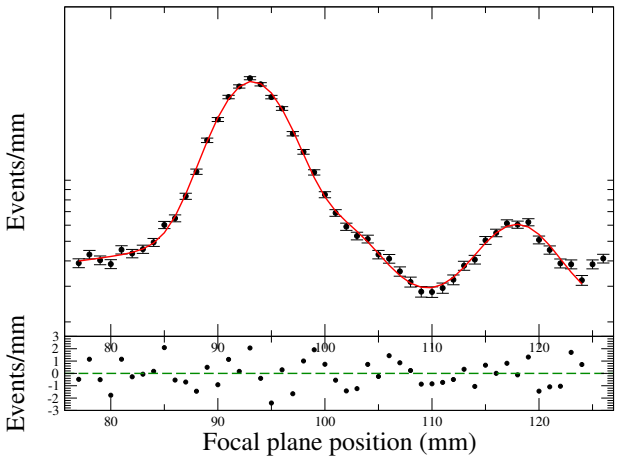
Events/mm
Events/mm
Focal plane position (mm)

Table A.1: The measured position centroids and areas for the triton events at the focal plane.

μ_t (mm)	FWHM (mm)	Area (Counts)	χ^2_ν
662.98 ± 0.10	4.00 ± 0.22	668 ± 28	0.56
606.99 ± 0.05	4.42 ± 0.07	2946 ± 60	0.95
597.34 ± 0.04	4.42 ± 0.07	3439 ± 63	0.95
522.85 ± 0.01	3.98 ± 0.02	45822 ± 215	1.38
501.01 ± 0.05	3.98 ± 0.02	2288 ± 51	1.38
463.59 ± 0.07	4.39 ± 0.06	9781 ± 104	1.67
454.58 ± 0.07	4.39 ± 0.06	40442 ± 205	1.67
361.64 ± 0.08	4.89 ± 0.15	3695 ± 70	0.91
339.29 ± 0.08	3.81 ± 0.20	1134 ± 43	0.91
304.06 ± 0.05	4.63 ± 0.06	10674 ± 228	1.98
293.53 ± 0.04	4.63 ± 0.06	31973 ± 502	1.98
279.88 ± 0.23	5.46 ± 0.26	20060 ± 612	1.98
242.44 ± 0.20	9.47 ± 0.14	11606 ± 176	2.06
232.44 ± 0.23	4.22 ± 0.22	9345 ± 132	2.06
93.28 ± 0.05	7.47 ± 0.11	24474 ± 343	1.46

Appendix B

Energy loss of the recoil in the target

The program used for the energy loss calculation of the ^{24}Al recoils within a MgF_2 target is shown in Listing. B.1.

Listing B.1: A program that calculates the energy loss of an ion within a target.

```
#include <iostream>
#include <fstream>
#include <iomanip>
#include <cmath>
#include <math.h>

using namespace std;

const double light_speed = 3.E+08*1E-09; //Unit: um/fs

//Function prototype:
double Eloss_pol(double dx, double fit_pars[], double Erec);

int main()
{
    //Input parameters:
    ifstream fin1;
    fin1.open("fit_pars.dat");

    int RES;

    cout << "\nSpecify resonance: " << endl;
    cin >> RES;

    ofstream fout;
```

```
fout.open("Eloss_RES.dat");

//===== T a r g e t  I n f o r m a t i o n =====
double MgF2_aden = 200.; //Arial density ug/cm^2
double MgF2_den = 1.31960*1E+06; //Density ug/cm^3

//Obtain thickness in um from above:
double MgF2_thick;

MgF2_thick = (MgF2_aden/MgF2_den)*1E+04; //in um

cout << "MgF2_thick (um) = " << MgF2_thick << endl;

//Fit parameters from a polynomial fit to dE/dx versus Erec: Initialization
double fit_pars[5], fit_pars_err[5];

for (int i=0; i<4; i++)
{
    fin1 >> fit_pars[i] >> fit_pars_err[i];
}

//Kinetic energy and velocity (v/c):
double Erec[4] = {0.21018948,0.21528569,0.22345638,0.22593103}; //in keV
double Vrec[4] = {0.0043367865,0.0043890292,0.0044715147,0.0044961981};

//Calculated Energy loss:
double Elost, Eold, Enew;

//Initialize recoil energy:
Eold = Erec[RES-1];

//Number of slices:
long int Nr_slice = 1E+6;

//Slice Thickness:
double dx;

dx = (MgF2_thick/Nr_slice); //in um

fout << "dx (um) = " << dx << endl;

fout << "Ereduced \t Vrec  \t t_i = " << endl;

double t_old = 0., t_new = 0.;
double t_lifetime[4] = {3.0192661,0.25781434,6.9278158E-04,0.019350856};
```

```
    int Slice_ctr = 0;

    do
    {
        Enew = Eold - Eloss_pol(dx,fit_pars,Eold);

        //Recoil velocity from kinetic energy:
        Vrec[RES-1] = sqrt(2*Enew/(22349.166*1E+03))*light_speed; //um/fs

        t_new = (t_old + (dx/(Vrec[RES-1])));

        cout << Enew << "\t" << Vrec[RES-1] << "\t" << t_new << endl;

        //Update energy and increment time:
        Eold = Enew;
        t_old = t_new;
        Slice_ctr++;
    }
    while(t_new<t_lifetime[RES-1]);

    //Range (um):
    fout << "Slice_ctr = " << Slice_ctr << "\t" << "Range (micron) = " << dx*Slice_ctr <<
    endl;

    cout << "\nNumber of slices = " << Slice_ctr << endl;

    double Del_E;
    Del_E = Erec[RES-1] - Eold;

    fout << "Total energy loss in lifetime of the state: Delta_E (keV) = " << Del_E << endl;

    return 0;
}

//Eloss function:
double Eloss_pol(double dx, double fit_pars[], double Erec)
{
    double Elost = 0.0;

    Elost = (fit_pars[0] + fit_pars[1]*Erec + fit_pars[2]*pow(Erec,2) + fit_pars[3]*pow(Erec
    ,3))*dx;

    return Elost;
}
```

Bibliography

[1] C. E. Rolfs and W. S. Rodney, *Cauldrons in the Cosmos*. The University of Chicago, Chicago, 1988.

[2] C. Bertulani, *Nuclei in the Cosmos*. World Scientific, 2013.

[3] M. A. Seeds, *Horizons: Exploring the Universe*. Brooks/Cole, 2003.

[4] C. Iliadis, *Nuclear Physics of Stars*. Wiley & Sons, 2008.

[5] S. M. Couch, "The mechanism(s) of core-collapse supernovae," *Philosophical Transactions of the Royal Society A: Mathematical, Physical and Engineering Sciences*, vol. 375, no. 2105, p. 20160271, 2017.

[6] `https://www.astroart.org/extrasolar?lightbox=image_ixa`.

[7] M. Politano, S. Starrfield, J. Truran, A. Weiss, and W. Sparks, "Hydrodynamic studies of accretion onto massive white dwarfs: ONeMg-enriched nova outbursts. I. Dependence on white dwarf mass," *The Astrophysical Journal*, vol. 448, p. 807, 1995.

[8] M. Wiescher, J. Görres, E. Uberseder, G. Imbriani, and M. Pignatari, "The Cold and Hot CNO Cycles," *Annual Review of Nuclear and Particle Science*, vol. 60, no. 1, pp. 381–404, 2010.

[9] L. Erikson *et al.*, "First direct masurement of the ^{23}Mg$(p,\gamma)^{24}$Al reaction," *Phys. Rev. C*, vol. 81, p. 045808, Apr 2010.

[10] F. Hammache, "Introduction to experimental nuclear astrophysics." `https://indico.tlabs.ac.za/event/105/contributions/2069/`.

[11] L. Trache, "Indirect Methods For Nuclear Astrophysics With Radioactive Nuclear Beams," *AIP Conference Proceedings*, vol. 1213, 03 2010.

[12] G. R. Satchler, *Direct nuclear reactions*. 1983.

[13] B. Bransden and C. Joachain, *Quantum Mechanics*. Pearson Education, 2000.

[14] C. Iliadis and M. Wiescher, "Spectroscopic factors from direct proton capture," *Physical Review C*, vol. 69, no. 6, p. 064305, 2004.

[15] R. Wallace and S. E. Woosley, "Explosive hydrogen burning," *The Astrophysical Journal Supplement Series*, vol. 45, pp. 389–420, 1981.

[16] C. Lederer and V. Shirley, "Table of Isotopes," 1978.

[17] M. Wiescher, J. Gorres, F.-K. Thielemann, and H. Ritter, "Explosive hydrogen burning in novae," *Astronomy and Astrophysics*, vol. 160, pp. 56–72, 1986.

[18] M. B. Greenfield *et al.*, "The ^{24}Mg(^{3}He,t)^{24}Al reaction and $L = 1$ giant resonance systematics using an effective ^{3}He-n interaction at 27 MeV/nucleon," *Nuclear Physics A*, vol. 524, no. 2, pp. 228–250, 1991.

[19] S. Kubono *et al.*, "Structure of ^{24}Al for the stellar reaction rate of ^{23}Mg(p,γ)^{24}Al," *Nuclear Physics A*, vol. 588, no. 2, pp. 521–536, 1995.

[20] H. Herndl *et al.*, "Thermonuclear reaction rate of ^{23}Mg$(p, \gamma)^{24}$Al," *Phys. Rev. C*, vol. 58, pp. 1798–1803, Sep 1998.

[21] S. Triambak, A. Garcia, D. Melconian, M. Mella, and O. Biesel, "Excitation energies in ^{33}Cl via ^{32}S(p, γ)," *Physical Review C*, vol. 74, no. 5, p. 054306, 2006.

[22] M. Kamil *et. al*, "Isospin mixing and the cubic isobaric multiplet mass equation in the lowest $T = 2$, $A = 32$ quintet," *Physical Review C*, vol. 104, no. 6, p. L061303, 2021.

[23] D. W. Visser *et al.*, "Measurement of ^{23}Mg(p,γ)^{24}Al resonance energies," *Physical Review, C (Nuclear Physics)*, vol. 76, 1 2007.

[24] G. Lotay *et al.*, "First in-beam γ-ray spectroscopy study of ^{24}Al and its implications for the astrophysical ^{23}Mg$(p, \gamma)^{24}$Al reaction rate in one novae," *Phys. Rev. C*, vol. 77, p. 042802, Apr 2008.

[25] R. Neveling *et al.*, "High energy-resolution zero-degree facility for light-ion scattering and reactions at iThemba labs," *Nuclear Instruments and Methods in Physics Research Section A: Accelerators, Spectrometers, Detectors and Associated Equipment*, vol. 654, pp. 29–39, Oct 2011.

[26] P. Adsley *et al.*, "CAKE: the coincidence array for K600 experiments," *Journal of Instrumentation*, vol. 12, pp. T02004–T02004, Feb 2017.

[27] W. R. Leo, *Techniques for Nuclear and Particle Physics Experiments*. Springer-Verlag, 1987.

[28] T. Khumalo, "Low Pressure Focal Plane Detector for the K600: A Design Study.," Master's thesis, University of Zululand, 2020.

[29] K. Ching Wei Li, "Characterization of the pre-eminent 4-α cluster state candidate in ^{16}O," Master's thesis, University of Stellenbosch, 2015.

[30] `https://www.nndc.bnl.gov/qcalc/`.

[31] E. Henley and A. Garcia, *Subatomic Physics*. World Scientific Publishing, 2007.

[32] R. E. Phillips and S. T. Thornton, "A fortran program for relativistic kinematic calculations in two-body nuclear reactions," tech. rep., Oak Ridge National Laboratory, 1967.

[33] J. Honkanen, M. Kortelahti, J. Äystö, K. Eskola, and A. Hautojärvi, "Decay of ^{24}Al and ^{24}Alm to γ-ray and α-particle emitting states in ^{24}Mg," *Physica Scripta*, vol. 19, no. 3, p. 239, 1979.

[34] D. Visser, C. Wrede, J. Caggiano, C. Deibel, R. Lewis, A. Parikh, and P. Parker, "Addendum to "Measurement of ^{23}Mg$(p,\gamma)^{24}$Al resonance energies"," *Physical Review C*, vol. 78, no. 2, p. 028802, 2008.

[35] W. Huang, M. Wang, F. G. Kondev, G. Audi, and S. Naimi, "The AME2020 atomic mass evaluation (i). Evaluation of input data, and adjustment procedures," *Chinese Physics C*, vol. 45, no. 3, p. 030002, 2021.

[36] S. Singh, A. Jain, and J. K. Tuli, "Nuclear Data Sheets for A = 222," *Nuclear Data Sheets*, vol. 112, no. 11, pp. 2851–2886, 2011.

[37] B. Singh *et al.*, "Nuclear Data Sheets for A=218," *Nuclear Data Sheets*, vol. 160, pp. 405–471, 2019.

[38] S. Zhu and E. McCutchan, "Nuclear Data Sheets for A=214," *Nuclear Data Sheets*, vol. 175, pp. 1–149, 2021.

[39] J. Ziegler and J. Biersack, "Srim-2013 software package," 2013.

[40] `https://www.srim.org`.

[41] E. Sheldon and P. Marmier, *Physics of Nuclei and Particles*. No. v. 1 in Physics of nuclei and particles, Academic Press, 1969.

[42] M. Kamil, "Spectroscopy of proton unbound states in ^{32}Cl," Master's thesis, University of the Western Cape, 2019.

[43] D. Tilley, H. Weller, and C. Cheves, "Energy levels of light nuclei A = 16–17," *Nuclear Physics A*, vol. 564, no. 1, pp. 1–183, 1993.

[44] R. Longland, C. Iliadis, A. Champagne, J. R. Newton, C. Ugalde, A. Coc, and R. Fitzgerald, "Charged-particle thermonuclear reaction rates: I. Monte Carlo method and statistical distributions," *Nuclear Physics A*, vol. 841, no. 1-4, pp. 1–30, 2010.

[45] P. Endt, "Supplement to energy levels of a= 21–44 nuclei (vii)," *Nuclear Physics A*, vol. 633, no. 1, pp. 1–220, 1998.

[46] R. G. T. Zegers *et al.*, "Spectroscopy of ^{24}Al and extraction of gamow-teller strengths with the ^{24}Mg(^{3}He,t) reaction at 420 MeV.," *Phys. Rev. C*, vol. 78, p. 014314, 2008.

[47] C. Iliadis, R. Longland, A. Champagne, and A. Coc, "Charged-particle thermonuclear reaction rates: Iii. Nuclear physics input," *Nuclear Physics A*, vol. 841, no. 1-4, pp. 251–322, 2010.